3-2022

Formulation and Characterization of Fast-Curing Plastic Scintillators with High-Z Loading

Theodore W. Stephens

FORMULATION AND CHARACTERIZATION OF FAST-CURING PLASTIC SCINTILLATORS WITH HIGH-Z LOADING

THESIS

Theodore W. Stephens, Lieutenant Colonel, USA

AFIT-ENP-MS-22-M-112

DEPARTMENT OF THE AIR FORCE
AIR UNIVERSITY

AIR FORCE INSTITUTE OF TECHNOLOGY

Wright-Patterson Air Force Base, Ohio

AFIT-ENP-MS-22-M-112

FORMULATION AND CHARACTERIZATION OF FAST-CURING PLASTIC SCINTILLATORS WITH HIGH-Z LOADING

THESIS

Presented to the Faculty

Department of Engineering Physics

Graduate School of Engineering and Management

Air Force Institute of Technology

Air University

Air Education and Training Command

in Partial Fulfillment of the Requirements for the

Degree of Master of Science in Nuclear Engineering

Theodore W. Stephens, B.A, M.S.

Lieutenant Colonel, USA

March 24, 2022

AFIT-ENP-MS-22-M-112

FORMULATION AND CHARACTERIZATION OF FAST-CURING PLASTIC SCINTILLATORS WITH HIGH-Z LOADING

THESIS

Theodore W. Stephens, B.A, M.S.
Lieutenant Colonel, USA

Committee Membership:

LTC Andrew W. Decker, Ph.D
Chair

Juan J. Manfredi, Ph.D
Member

John W. McClory, Ph.D
Member

AFIT-ENP-MS-22-M-112

Abstract

Development of novel fast-curing plastic scintillators is highly advantageous due to their potential application in 3D-printed pixelated arrays. The printing of arrays for radiation detection and localization purposes is expected to significantly reduce the current manufacturing time, labor, and cost involved when compared to traditional methods while also producing superior geometric uniformity and light collection. Several formulations were developed that exhibit enhanced photon sensitivity, producing modest but discernible photopeaks at an incident gamma energy of 122 keV. The photon sensitivity is achieved via bismuth high-Z loading; however, this practice typically results in diminished light yields. For example, the inclusion of 10wt% triphenyl bismuth ($BiPh_3$) in a pilot formulation resulted in a light yield of ∼40% compared to a control formulation without bismuth. This depressed light yield was minimized in later samples by reducing the bismuth loading, thereby investigating the trade-off between light yield and detection efficiency. Subsequent formulations, which varied the photoinitiator concentration and curing time, demonstrated successful curing with sufficient plastic hardness, reduced purple discoloration, reduced heat buildup during curing, and resulted in less cracking during the curing process, all of which were correlated with lower concentrations of the photoinitiator. These scintillators, however, did exhibit appreciable leaching of the primary fluorophore and those with the lowest concentration of photoinitiator (i.e., 0.01 wt%) developed surface fissuring within the first few weeks after curing. As compared to EJ-256 with ^{137}Cs and ^{57}Co sources, relative light yield was generally slightly poorer, ranging from 42% to 93%, and relative efficiency was generally comparable, ranging from 47% to 167%.

Table of Contents

Page

List of Figures

Figure Page

List of Tables

Table Page

FORMULATION AND CHARACTERIZATION OF FAST-CURING PLASTIC SCINTILLATORS WITH HIGH-Z LOADING

I. Introduction

1.1 Applications of Plastic Scintillators

Plastic scintillators are widely employed in many radiation detection applications, particularly in situations requiring large detector volumes, such as radiation portal monitors [4, 5]. Despite offering excellent fast neutron sensitivity, unsensitized plastic detectors typically require augmentation by other detectors with greater photon sensitivity and finer resolution to provide a more complete radiological characterization of monitored materials [3].

Plastic scintillators also offer an attractive option for applications in which assemblies of multiple detector bodies (e.g., pixelated arrays) are required [6]. Pixelated arrays have utility in industrial imaging and medical tomography, where precise spatial resolution is necessary. These may be used in conjunction with digital thin-film transistor arrays or position-sensitive photomultiplier tubes to preserve positional information on incident radiation and, thus, produce high-resolution imaging in applications such as positron emission tomography (PET), gamma camera imaging, or flash radiography [7, 8]. In many situations, especially where safety and security is of concern, detectors with dual-particle imaging (DPI) capabilities could be of great utility [9].

The attractiveness of plastic scintillators for such applications is due to the relatively low cost of constituent materials and the ability to easily fabricate singular

detector bodies in a broad range of shapes and sizes. In contrast, the traditional production methods for pixelated plastic scintillator arrays are typically tedious, time-consuming, and expensive. Construction of pixelated arrays entails precision cutting and machining of individual scintillator rods (often with dimensions on the order of millimeters), polishing, wrapping with reflective material, and assembly into arrays of various dimensions, often containing as many as 10×10 (or even more) individual scintillator rods [10]. Consequently, the existing methods for pixelated array construction are typically expensive in terms of time and cost, especially when geometric uniformity is maximized. Therefore, investigation into novel, fast-curing plastic scintillator formulations usable in 3D printing machines may provide an improved means of producing plastic pixelated arrays in a more efficient manner, both in terms of cost and time, while also ensuring a higher degree of geometric precision in the arrays.

The term "fast-curing" is used to describe plastic scintillator formulations that cure on the order of minutes or hours. The required cure times can be as low as a few minutes when photocuring techniques are implemented, such as those using high-intensity light at a suitable wavelength [11], typically in the range of 300-500 nm. This "fast-curing" method is distinguishable from more conventional "slow-curing" approaches that apply to plastic formulations requiring cure times on the order of several hours to several days. Slow-curing formulations often require the the application of heat in special ovens to implement the curing process, whereas fast-curing formulations, such as the ones explored in this investigation, only require exposure to a specific wavelength of light (due to the action of a chemical photoinitiator) and no exogenous heat source.

Regarding detection capabilities, plastic scintillator arrays offer superior detection of fast neutrons. Of course, plastic scintillator arrays are not expected to replace high-efficiency and high-resolution systems optimized for x-ray detection, such as modern

solid-state arrays with sub-200 μm pixel sizes. Fast-curing plastic scintillator formulations are, however, expected to improve the fabrication processes and geometric precision of larger, lower resolution arrays, all while substantially reducing the time and cost of production. Plastic scintillator arrays will never replace solid-state arrays due to the longer mean free path of photons in plastic when compared to other materials with higher electron densities. Additionally, traditional plastic scintillator formulations, i.e., those utilizing a polyvinyl toluene (PVT) or polystyrene (PS) base, are impractical for 3D printing production methods due to their associated slow rates of curing. Consequently, any novel fast-curing plastic scintillator formulation that offers a broad range of performance characteristics could potentially be of substantial utility and contribute to the state of the art in this field.

1.2 Research Objectives

In this investigation, novel plastic scintillators are fabricated using new combinations of monomers, crosslinkers, chromophores, fluorophores, photointitiators, and high-Z compounds to facilitate the fast-curing polymerization process and explore viable scintillator detection media. The rapid polymerization and curing process employs photocuring techniques, which utilize high-intensity light in the blue to ultraviolet region of the elecromagnetic spectrum to rapidly cure and solidify the scintillator body.

The intent of this study is to formulate and produce a fast-curing plastic scintillator capable of comparable photon sensitivity and light yield relative to high-Z-loaded commercially available plastic. The fast-curing nature of the scintillator would make it an attractive candidate for 3D printing applications, in which materials are fabricated rapidly in iterative cycles. The measured performance characteristics are

compared to a commercial standard produced by Eljen Technology, EJ-256, which is a PVT-based plastic loaded with 5 wt% lead (Pb). The published performance metrics for EJ-256 is provided in Table 1 [12].

Table 1: Commercial Plastic Scintillator Characteristics

Characteristics	**EJ-256**
Light Output (%Anthracene)	34
Scintillation Efficiency (photons / 1 MeVee)	5,200
Wavelength of Maximum Emission (nm)	425
Density g/cm^3	1.081
High-Z Additive (wt%)	Lead (5)

1.3 Document Overview

This document is organized as follows: Chapter II provides an overview of relevant background information and theory regarding scintillator detection. Chapter III details the methods, practices, processes, and procedures employed in the conduct of this investigation. Chapter IV presents the results and analysis of the findings concerning scintillator formulation and characterization. Finally, Chapter V discusses the conclusions drawn from the analysis and proposes several potential research areas for future work.

II. Background & Theory

2.1 Scintillator Overview

Scintillator radiation detectors convert incident ionizing radiation into photons emitted in or near the visible spectrum that are then measured in a photodetector. This process begins with the excitation of the detector material, which is initiated by the interaction of incident photons, neutrons, or charged particles within the scintillator material. Incident charged particles react directly with the scintillator media, while photons typically interact with orbital electrons and fast neutrons typically scatter elastically off atomic nuclei in the scintillator, thereby creating charged recoil particles. These interactions result in numerous ionization or excitation events which lead to molecular de-excitations that emit the optical photons converted into an electric signal by a photodetector.

Traditional scintillators may be broadly categorized as organic or inorganic, depending on the chemical nature of the detection medium. Inorganic scintillators operate via a charged particle (e.g., an electron resulting from photoelectric interaction with an incident photon) creating electron-hole pairs along its path in the detector. In a pure inorganic crystal, the radiative de-excitation of a conduction band electron back to the valence band may be an inefficient process, which can be mitigated by addition of a dopant to modify the energy structure at the dopant sites, as shown in Figure 1 [13]. When an activator is present, the holes preferentially migrate through the crystal lattice of the detector medium to an activator (i.e., dopant) site due to the lower ionization energy at the site compared to non-activated sites. The electron of the electron-hole pair, which has been elevated to the conduction band due to the energy imparted to it by the charged particle, is free to move about the crystal until it reaches an ionized activator site. The recombined electron-hole pair can now de-

excite via photon emission [14]. The interconnected crystal structure of constituent elements in an inorganic scintillator is a key attribute of the scintillation mechanism, facilitating migration of electron-hole pairs throughout the medium toward a favorable location for de-excitation. Illustrations of such crystal structures for two common inorganic scintillators, sodium iodide (NaI) and barium fluoride (BaF_2), are shown in Figure 2. NaI scintillators are often doped with small amounts of an activator, such as thallium, and BaF_2 scintillators may be unactivated. Inorganic scintillators typically offer a very high light yield (with some, such as LuI_3:Ce and SrI_2:Eu, observed with light yields as high as 100,000 photons / MeV), often exhibit negligible reabsorption of scintillation light, and generally provide significant photoelectric interaction (and, thus, full energy deposition) with incident photons [15, 16]. Inorganic scintillators have higher electron densities than organic scintillators due to their higher-Z constituent elements, leading to more interaction events and greater energy deposition of the high-energy recoil electrons. This results in a higher population of information carriers (in the form of scintillation photons) to more precisely resolve the incident particle energy. Consequently, inorganic scintillators are also typically characterized by higher resolution. Furthermore, the energy threshold required to generate a scintillation photon in a NaI(Tl) inorganic scintillator has been shown to be lower that that required for a NE-102A (analagous to EJ-212) standard plastic scintillator by a factor of 3.5 to 4 [17, 18]. Some drawbacks of inorganic scintillators are that they typically have no intrinsic ability to detect neutrons (requiring doping with a neutron sensitive material to gain this capability), have relatively slow response times on the order of 10^{-7} seconds, and are often sensitive to moisture in the environment [19].

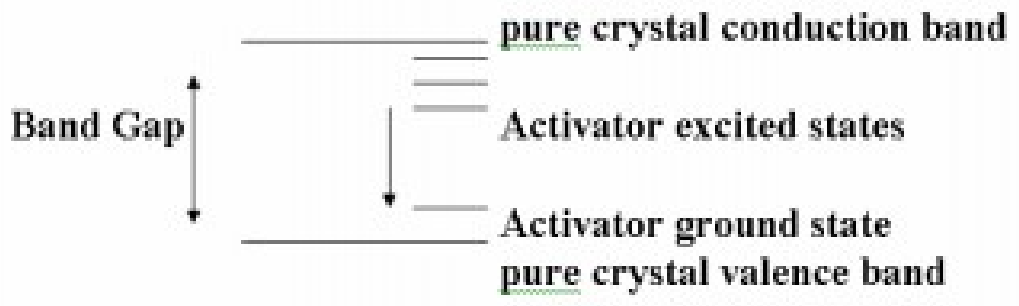

Figure 1: Inorganic Scintillator Energy Structure

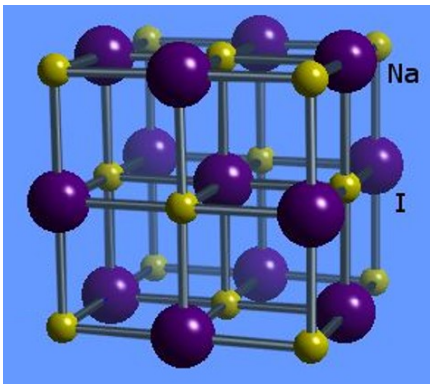

(a) Sodium Iodide

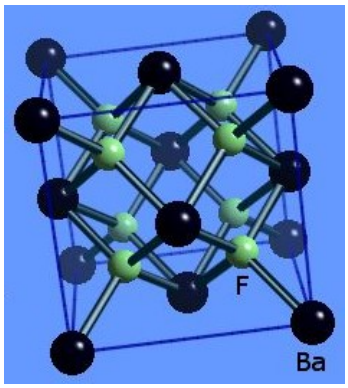

(b) Barium Fluoride

Figure 2: Inorganic Scintillator Crystal Structures

Organic scintillators operate via a different mechanism: individual molecules are excited by incident radiation and the subsequent deexcitation produces a photo-emission in the visible spectrum. This process is explained in greater detail in Section 2.2. Since the scintillation mechanism for organics operates on the molecular level, it can occur in any physical phase (as opposed to conventional inorganic scintillators, which must be in solid, crystalline phase). For this reason, organic scintillators are often divided into the subcategories of liquid (e.g., linear alkyl benzene [Figure 3a], deuterated benzene [Figure 3b]), crystal (e.g, anthracene [Figure 3c], stilbene [Figure 3d]), and plastic (e.g., polystyrene [Figure 3e], polyvinyltoluene [Figure 3f]). Organic liquids tend to be resistant to radiation damage and can measure low-energy radiation with high efficiency, especially when radioactive sources are dissolved or emulsified

within the detection medium; however, organic liquids are often volatile, flammable, environmentally unfriendly, and susceptible to degradation by dissolved oxygen if not kept completely sealed [19] [20]. Organic crystals offer the highest scintillation efficiency of any organic scintillators, but are very fragile and difficult to produce in large volumes [19]. Plastics may not possess the same level of performance characteristics or capabilities of other organic scintillators, but they are comparatively durable and are easy to produce in large volumes with various fabrication techniques [3]. Response time of organic scintillators is generally much faster than that of inorganic scintillators, with response times on the order of 10^{-9} seconds [14]. This quality makes organic scintillators better for characterizing high-activity sources and in situations where fine timing precision is desired. Some general drawbacks of organic scintillators, as compared to inorganic scintillators, are that they typically do not capture the full energy of incident photons, can often reabsorb scintillation photons, and exhibit comparatively poorer energy resolution [19].

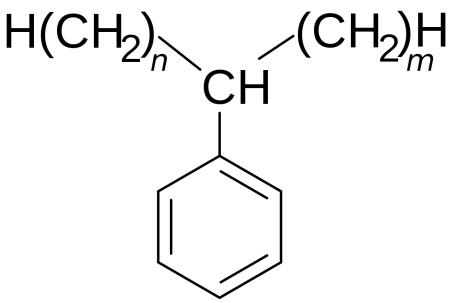

(a) Linear Alkyl Benzene

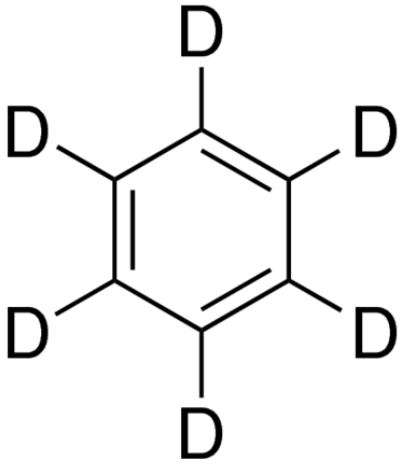

(b) Deuterated Benzene

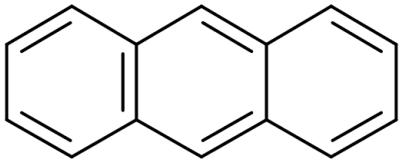

(c) Anthracene

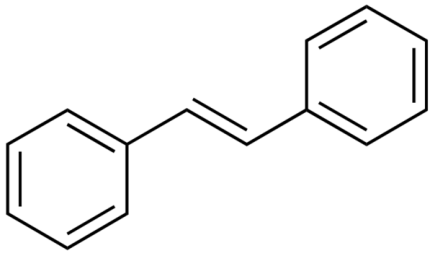

(d) Stilbene

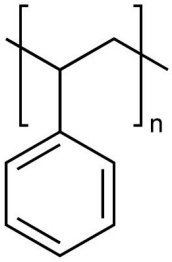

(e) Polystyrene

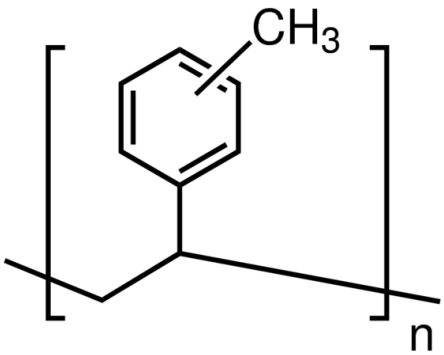

(f) Polyvinyltoluene

Figure 3: Examples of Organic Scintillators

This investigation explores the development of fast-curing, high-Z-loaded plastic scintillators that may provide appreciable photon sensitivity compared to non-high-Z-loaded plastics while maintaining sufficient light yield. Sensitivity refers to the likelihood that incident radiation particles interact with the detector material and produce radiant, measurable emissions. In this investigation, sensitivity is quantified as relative efficiency compared to EJ-256. Similarly, light yield is not quantified in absolute terms but as relative light yield compared to EJ-256. These metrics are defined in Section 2.2.6.

2.2 Organic Scintillator Function

An organic scintillating compound is composed of a hydrocarbon base with fluorophore dyes that fluoresce and/or phosphoresce following interaction with high-energy incident radiation. Incident photons and neutrons produce high-energy recoil electrons and protons, respectively. Molecular structures exhibiting conjugated bonding (e.g., phenylated compounds) can undergo electronic excitation from recoil electrons and protons in the matrix followed by radiative de-excitation in the form of scintillation photon emission in the visible region of the electromagnetic spectrum, known as radioluminescence. Scintillation photons that are emitted from the scintillator body to the PMT are subsequently converted to photoelectrons by a photocathode. Photoelectrons are produced by the photocathode at varying levels of quantum efficiency, which is defined as the ratio of photoelectrons produced to the number of photons impacting the photocathode. Quantum efficiency is primarily dependent on scintillation photon wavelength and photocathode composition. The photoelectrons are amplified in the PMT by a series of dynodes, each of which is maintained at a higher magnitude of electric potential than the previous one. Each dynode emits multiple electrons for each electron absorbed, thereby generating a current pulse at the

terminal anode that is significantly greater in magnitude than the pulse originating at the photocathode and subsequently generating the detector response output. This process is illustrated in Figure 4 [21].

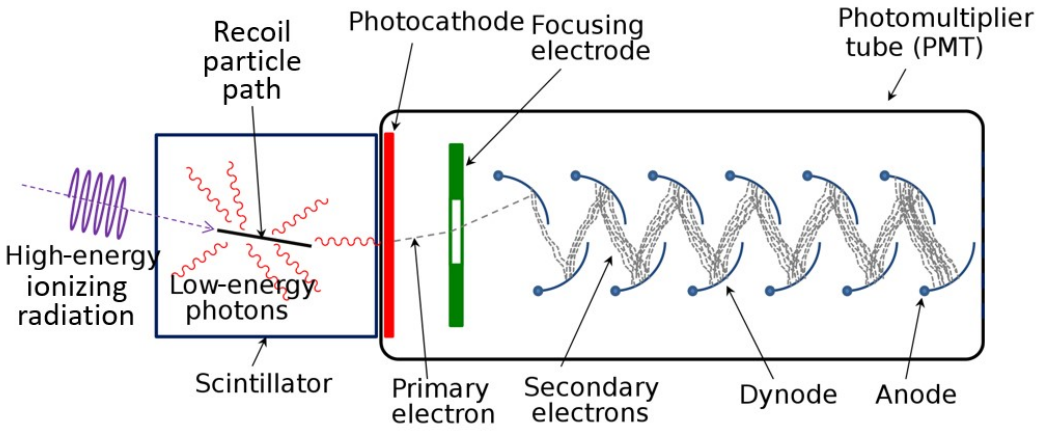

Figure 4: Process of Irradiation, Scintillation, and Current Amplification

2.2.1 Plastic Scintillator Raw Materials

Raw materials for plastic scintillator formulation include monomers, crosslinkers, fluorophores, waveshifters, photoinitiators, and high-Z compounds. Monomers are the individual molecules that bond together to form polymer chains upon curing. The monomer used in this investigation is isobornyl acrylate (IBOA). IBOA is utilized due to its ability to be cured on "fast" timescales (i.e., seconds to minutes). However, as can be seen from its molecular structure in Figure 5, it lacks any aromatic ring structure (i.e., conjugated bonding), so it is of limited use as a light-harvesting chromophore. This characteristic distinguishes IBOA from more conventional plastic scintillator bases, such as polystyrene (PS) or polyvinyl toluene (PVT), which do not support fast-curing formulations.

Crosslinkers are the compounds that link the polymer chains together, thereby enhancing structural integrity. The crosslinkers used in this investigation are 1,6-hexanediol dimethacrylate (HDDMA) (Figure 6) and bisphenol A dimethacrylate

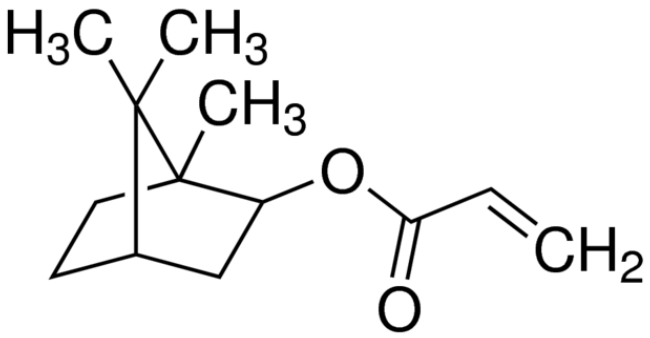

Figure 5: Isobornyl Acrylate (IBOA)

(BPADM) (Figure 7). Previous studies have indicated that HDDMA is advantageous for clarity (i.e., long attenuation length) but less than optimal for hardness, while BPADM has been shown to be advantageous for hardness but less than optimal for clarity [1]. These observations have been revealed via empirical study, although the underlying mechanisms responsible for these characteristics are still not fully understood.

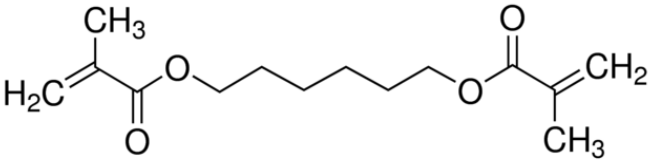

Figure 6: 1,6-Hexanediol Dimethacrylate (HDDMA)

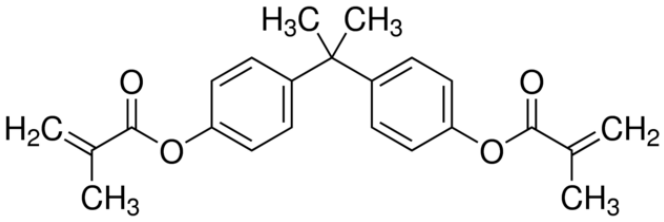

Figure 7: Bisphenol A Dimethacrylate (BPADM)

Fluorophores are materials that exhibit electronic de-exciattion via photon emission. Since increased photon emission results in enhanced light yield and, hence,

improved scintillator performance, it is advantageous to optimize scintillator fluorescence. The primary fluorophore utilized in this investigation was 2,5-diphenyl oxazole (PPO) (Figure 8). Previous investigations demonstrated that scintillators utilizing PPO exhibit appreciable fluorescence as well as pulse shape discrimination (PSD) [1]. A few formulations also used diisopropyl naphthalene (DIPN) (Figure 9), which is an aromatic solvent used in the preparation of the commercial liquid scintillator EJ-309 [22]. DIPN was selected for use in this investigation due to its established record of performance as a functional fluorophore [23]. Furthermore, a close analog of DIPN (naphthalene), has been shown to reduce the quenching effect of high-Z organometallic additives in plastic scintillator formulations [14].

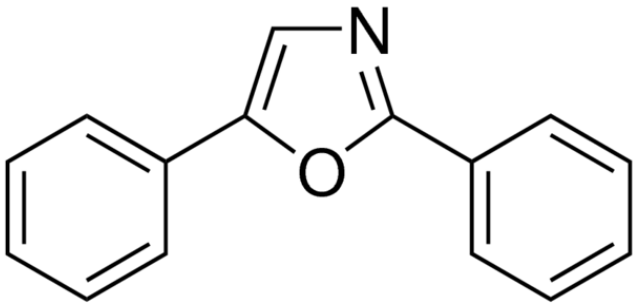

Figure 8: 2,5-Diphenyloxazole (PPO)

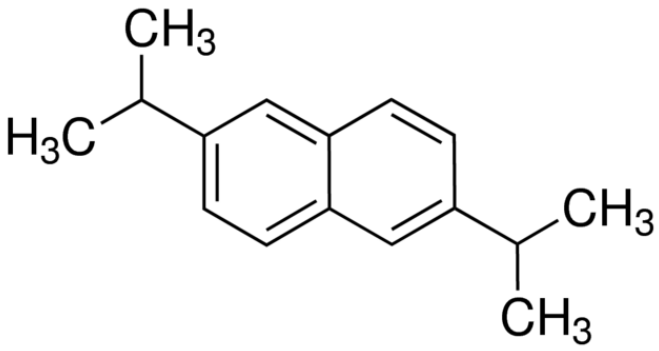

Figure 9: Diisopropyl Naphthalene (DIPN)

Photoinitiators are compounds that create reactive species when exposed to radiation, typically in the UV to visible region of the electromagnetic spectrum. The pho-

toinitiator employed in this investigation is diphenyl (2,4,6-trimethylbenzoyl) phosphine oxide (TPO) (Figure 10). TPO is cleaved into benzoyl and phosphinoyl radicals upon exposure to light in the wavelength range of 380-410 nm, which includes long wavelength UV to visible violet light (Figure 11). In this investigation, we employ 405 nm light for curing. Both radicals contribute to polymerization (i.e., curing) of the monomer. The phosphinoyl radical is approximately twice as reactive as the benzoyl radical, but it is readily converted to the low-reactivity peroxy radical upon exposure to O_2 [24]. This is one of the main reasons that sparging with inert gas (i.e., N_2) is conducted to displace dissolved O_2 in the scintillator formulations prior to curing. The presence of dissolved O_2 is also unfavorable because it provides an additional pathway for non-radiative quenching of excited states, thereby contributing to decreased fluorescence [19].

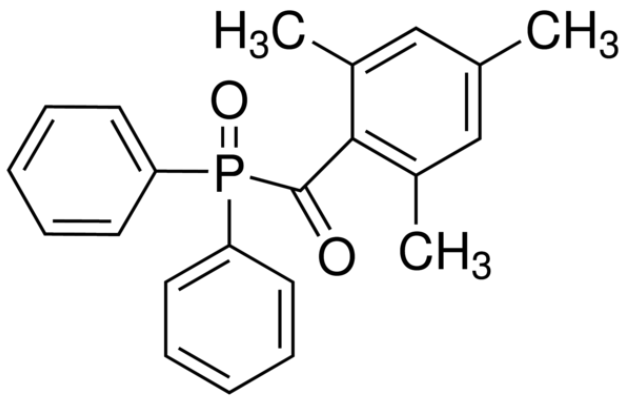

Figure 10: Diphenyl (2,4,6-Trimethylbenzoyl) Phosphine Oxide (TPO)

Waveshifters, or secondary dyes, are a subset of fluorophores employed to alter the wavelength of emitted photons from that of the absorbed photon. If scintillation photons emitted by the primary fluorophore are also readily absorbed by it, which can occur whenever appreciable overlap exists between the absorption and emission spectra, then light production is reduced. Additionally, the emitted scintillation photons may be characterized by a wavelength not optimally matched to exploit the peak

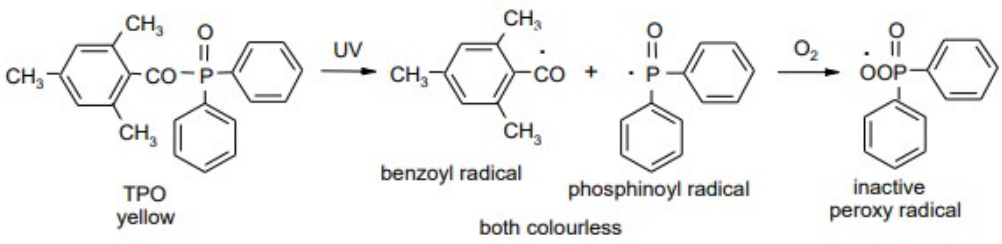

Figure 11: TPO Photo-Induced Radicalization Reaction

quantum efficiency of the photocathode. Both of these potential problems can be mitigated by utilizing a waveshifter in the scintillator formulation. The waveshifter absorbs light emitted by the primary fluorophore and re-emits photons at a wavelength (usually in the visible range of the electromagnetic spectrum) that is not likely to be reabsorbed in the scintillator. Waveshifters can effectively be employed in relatively low concentrations, often in the range of 0.005-0.5 wt% [3]. The waveshifter employed in this investigation is the proprietary Exalite 416 (Figure 12), produced and distributed by Essilor/Luxottica. With the addition of Exalite 416 to the scintillator formulations, the peak emission wavelength occurs at 416 nm, as shown by the emission spectrum of a fast-curing plastic scintillator from a previous investigation (AFIT 130) in Figure 13 [1]. The emission spectrum also indicates an increase in emissive intensity with additional curing, which provided the impetus to investigate the effects of varying photoinitiator concentration and curing time.

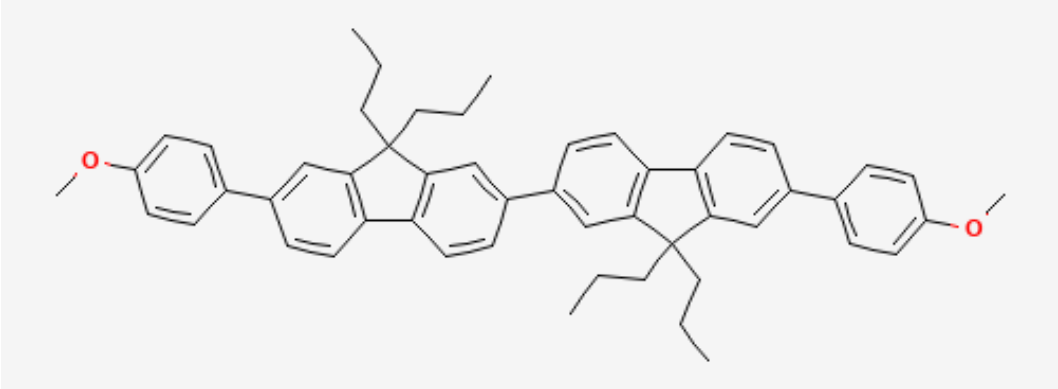

Figure 12: 7,7'-Di(4-Anisyl)-9,9,9',9'-Tetrapropyl-2,2'-Bi-9H-Fluorene (Exalite 416)

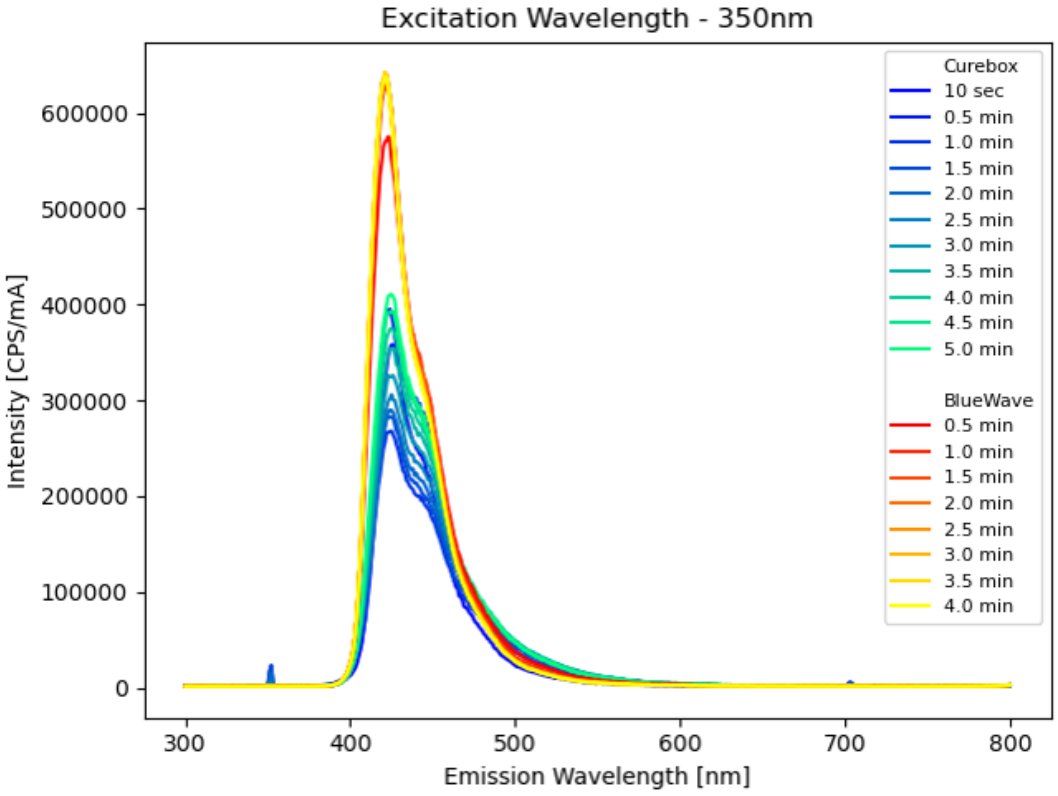

Figure 13: AFIT 130 Emission Spectrum During Curing Procedure [1]

2.2.2 Photon Detection

Due to the relatively low atomic number of the constituent materials (i.e., mostly hydrogen and carbon), unsensitized plastic scintillators typically suffer from a low

intrinsic efficiency for photoelectric absorption and may not produce a photopeak for incident particle energies greater than a few hundred keV. Therefore, the dominant mode of interaction between incident high-energy photons and the scintillator is via Compton scatter with orbital electrons. Compton scatter occurs when an incident photon imparts a portion of its kinetic energy to an electron in the detector medium, thereby resulting in the emission of a Compton electron and a scattered photon. The energy of the Compton electron (E_e) is given by Equation 1 and that of the scattered photon (E'_{photon}) by Equation 2,

$$E_e = E_{photon} - \frac{E_{photon}}{1 + (\frac{E_{photon}}{m_e c^2})(1 - cos\theta)} \tag{1}$$

$$E'_{photon} = \frac{E_{photon}}{1 + (\frac{E_{photon}}{m_e c^2})(1 - cos\theta)} \tag{2}$$

where E_{photon} is the energy of the incident photon, $m_e c^2$ is the rest mass energy of the electron (i.e., 511 keV), and θ is the angle of deflection of the scattered photon relative to the incident photon trajectory [19].

As can be seen from Equation 1, the maximum energy transferable from an incident photon to an electron via Compton scatter is appreciably less than the incident photon energy. This maximum energy imparted to the recoil electron, corresponding to a scatter angle (θ) of 180°, is known as the Compton edge energy. A Compton edge is distinguishable from a photopeak, which is an energy spectrum feature corresponding to absorption of the full energy of the incident particle. Since an incident photon $>\sim$ 200 keV will not typically deposit its full energy in an unsensitized plastic scintillator, a distinguishable photopeak is not usually observed. The inclusion of high-Z elements in plastic scintillator formulations, however, has been shown to increase their intrinsic efficiency for photon detection, thereby increasing the likelihood of observing

a photopeak and improving the utility of high-Z loaded plastic scintillators for photon spectroscopy [25]. Previous studies have successfully employed tin, lead, and bismuth for this purpose [26] [27]. The inclusion of high-Z elements, however, does also introduce the possibility of x-ray escape peaks being observed in the energy spectra, with the Kα escape peak often the most prominent due to its relatively high energy and rate of occurrence [28]. The Kα escape peak can coincide with other spectrum features, thereby obfuscating the results and preventing conclusive analysis.

2.2.3 Neutron Detection

Fast neutron detection in plastic scintillators is primarily achieved via recoil interactions with hydrogen, also known as neutron elastic scatter. In this process, incident neutrons colliding with hydrogen nuclei impart some or all of their energy in a reaction that conserves both momentum and kinetic energy within the detector medium. The resulting elastically-scattered recoil nuclei have energies given by Equation 3,

$$E_r = \frac{4A}{(1+A)^2}(cos^2\theta)E_n \tag{3}$$

where E_n is the incident neutron energy, A is the atomic number of the recoil nucleus, and θ is the scattering angle of the recoil nucleus with respect to the incident neutron trajectory [19]. The path created by the recoil proton induces ionization and excitation of atoms and molecules along its direction of travel.

This method of neutron detection requires incident neutrons of sufficient minimum energy. Hydrogen does not exist freely in organic media, but is typically bonded to another atom (commonly carbon) as a molecular constituent. Typical carbon-hydrogen bond energies are in the range of 3-5 eV. Furthermore, to create a charged particle (i.e, proton), the hydrogen atom must be ionized, which requires at least 13.6 eV. Therefore, an incident neutron must have an energy on the order of at

least tens of eV in order to induce a proton recoil reaction. This means that low-energy neutrons, including thermal neutrons (with a mean energy of 0.025 eV) will not be detected via this process. If sensitivity to low-energy neutrons is desired, one method of accomplishing this would be to include a material in the scintillator matrix with an appreciable cross-section for interaction with low-energy neutrons, e.g., lithium-6, boron-10, or a fissile material. In practice, organic scintillators that are unsensitized for low-energy neutrons can produce recoil protons with energies as low as 50 keV. Typical uses for unsensitized organic scintillators include detection of neutrons resulting from fission events, with energies of ∼1-2 MeV, or from neutron generators, with energies of ∼2.5 MeV (for D-D reactions) or ∼14.1 MeV (for D-T reactions).

2.2.4 Scintillator Interactions with Radiation and Associated Processes

The introduction of an incident high-energy photon or neutron into a plastic scintillator can result in recoil interactions, producing a high-energy electron or proton, respectively. The recoiling charged particle will create an ionization track within the scintillator, leaving a trail of excited and/or ionized molecules in its wake.

The partially ionized molecules rapidly recombine with free electrons to either excited singlet (S) or triplet (T) states in a 1:3 (singlet:triplet) ratio, according to spin statistics. The population of singlet and triplet states is also impacted by the energy loss per unit path length (dE/dx) of the recoiling particle. The rate of energy loss and, thus, ionization density, is greater for a recoiling proton than for a recoiling electron. Greater ionization density increases quenching (i.e., non-radiative energy transfer or loss), which competes with prompt fluorescence of S_1 states. Quenching includes (but is not limited to) the following processes, in which excited states become ionized,

$$S_n + S_m \rightarrow S_0 + I^+ + e^- \tag{4}$$

$$S_n \rightarrow I^+ + e^- \tag{5}$$

where S_n and S_m are excited singlet states, I^+ is a positively charged ion, and e^- is a free electron. In these cases, the interaction of two excited singlet states produces a singlet ground state and an ion pair (Equation 4) or the interaction of an excited state with an electric field generated by nearby ions produces an ion pair (Equation 5) [3]. When the ions recombine, they are three times as likely to form triplet states than singlet states, due to the aforementioned spin statistics and, thus, produce less fluorescence.

Quenching also competes with internal conversion, which converts highly-excited singlet states down to the S_1 state, i.e., the first excited singlet state. Within the S_1 state, several excited vibrational states S_{1x} are possible, and these relax via non-radiative processes to the S_{10} state. Internal conversion and vibrational relaxation occur very rapidly, on the order of femtoseconds to picoseconds. S_{10} states can de-excite radiatively, emitting a photon, resulting in prompt fluorescence. Prompt fluorescence, which typically occurs on the order of a few nanoseconds after excitation, is the main radiative de-excitation pathway by which organic scintillators operate.

Regarding excited states, there are several energy transitions that can occur to facilitate a subsequent return to the ground energy state. Many of these pathways compete with prompt fluorescence for de-excitation, both radiatively (i.e., photon-producing) and non-radiatively (i.e., non-photon-producing). Delayed fluorescence and phosphorescence are radiative de-excitation pathways with luminescent decay timescales on the order of tens/hundreds of nanoseconds or milliseconds, respectively, as opposed to ones of nanoseconds for prompt fluorescence. Although it is not typ-

ically observed in conventional organic scintillators, the non-radiative process of intersystem crossing could theoretically convert some excited singlet states S_1 to the excited triplet state T_1. In most organic scintillators, however, the population of T_1 states is produced almost entirely via ion recombination. The direct de-excitation of T_1 to S_0, which could proceed radiatively (resulting in phosporescence) or non-radiatively, is not observed to occur in conventional organic scintillators [29]. Such a transition would necessitate a spin flip (so as to not violate the Pauli Exclusion Pricniple), but the presence of a material that facilitates spin-orbit coupling (e.g., an iridium-complex fluorophore) would be necessary to make this process favorable [3]. T_1 states may also interact with each other via the energy transfer mechanism of triplet-triplet annihilation (TTA), shown in Equation 6, resulting in a S_0 state and a S_1 state. The S_1 state may then radiatively de-excite resulting in delayed fluorescence, which occurs on the order of microseconds.

$$T_1 + T_1 \rightarrow S_0 + S_1 \tag{6}$$

Other energy transition pathways that compete with fluorescence include non-radiative relaxation and quenching transitions to S_0 and radiative migration, by which a scintillation photon is reabsorbed after being emitted, prior to reaching the photocathode. In the case of radiative migration, the original characteristic excitation energy can be lost or degraded due to multiple absorptions and emissions [14]. Figure 14 illustrates some of the phenomena discussed in this section.

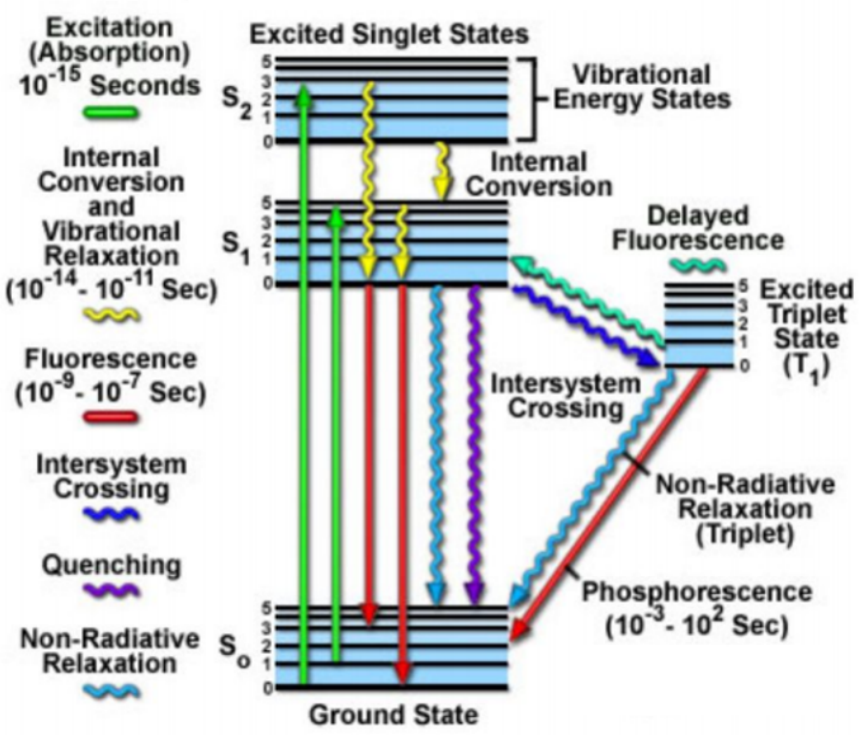

Figure 14: Excitation, De-excitation, and Energy Transfer Pathways [30]

The amount of incident radiation converted to radiative emission can be quantified by scintillation efficiency, i.e., the proportion of incident particle energy that is converted to light, which depends on both incident particle type and energy [14]. For incident particles of the same energy, recoil electrons (produced by photon interactions) are characterized by higher scintillation efficiency as compared to protons (produced by neutron interactions). This difference can be as much as an order of magnitude for incident particle energies up to several hundred keV, with the difference decreasing as energy increases. For this reason, the concept of absolute light yield is often used to address differences in scintillation efficiency for different particles. The term mega-electron volt electron equivalent (MeVee) is used to express the light yield corresponding to a 1 MeV electron. For a proton to produce equivalent light yield, its energy must be greater than 1 MeV due to the higher likelihood of non-radiative de-excitation pathways (resulting from greater ionization density, excited

state interactions, and triplet state occurrences) associated with proton interaction in the medium. Further complicating matters is the fact that light yield does not necessarily scale linearly with particle energy [14, 31]. Notwithstanding, linearity is sometimes assumed as an approximation.

2.2.5 Light Collection Enhancement

Several factors may be adjusted to improve light collection, both internal and external to the scintillator. Concerning external enhancement, light collection can be enhanced by optimizing factors concerning reflection and refraction, since photoemissions occur isotropically. Scintillation photons that exit the system will, obviously, not contribute to measurable light yield; therefore, all scintillator surfaces not interfacing with the PMT window are covered in layers of reflective material in order to retain scintillation photons in the system that might otherwise escape and redirect that emitted light back toward the photodetector. Additionally, the scintillator surface interfacing with the PMT window is coated with a material to maintain a consistent refractive index between the scintillator and PMT window, thereby optimizing transmittance of scintillation photons to the PMT.

Concerning internal enhancement, inclusion of appropriate fluorophores can also significantly improve light yield. These fluorophores typically provide a partially overlapping absorption spectrum with the emission spectrum of the organic base (or other light-harvesting elements in the formulation), thereby facilitating non-radiative energy transfer (e.g., Förster Resonance Energy Transfer (FRET), illustrated in Figure 15). FRET occurs via non-radiative dipole-dipole coupling from an electronically excited donor chromophore to an acceptor chromophore. The efficiency of FRET is increased by proximity of donor and acceptor chromophores, overlap of donor emission wavelength and acceptor absorption wavelength, and dipole alignment [32]. This

non-radiative process can transfer energy to a fluorophore that often has greater scintillation efficiency than the initially excited compound. The primary fluorophore used in this investigation, PPO, has a peak emission wavelength of 355 nm [33]. Photons emitted at this wavelength, however, can be reabsorbed due to partial overlap of the absorption and emission spectra [34]. A secondary wavelength-shifter dye may be employed to produce scintillation photons at a lower wavelength, thereby mitigating reabsorption by the primary dye and/or producing scintillation photons at a wavelength corresponding to the optimal quantum efficiency range of the photocathode. For a wavelength-shifter to be effective at minimizing reabsorption, there should be appreciable separation between its peak absorption wavelength and its peak emission wavelength, known as a Stokes shift, as illustrated in Figure 16.

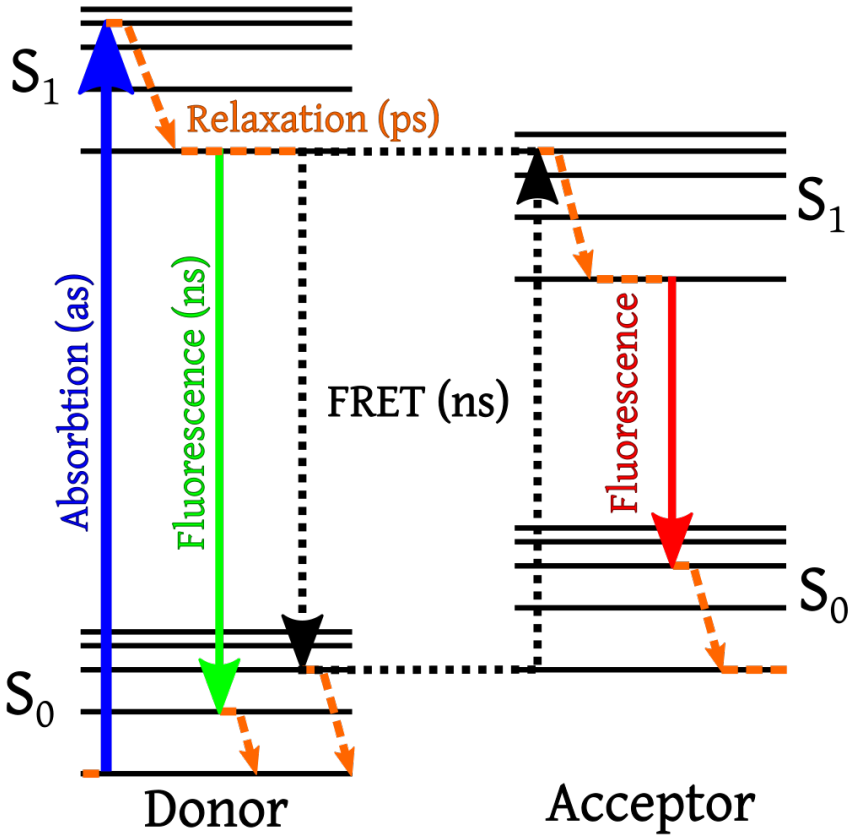

Figure 15: FRET Jablonski Diagram [35]

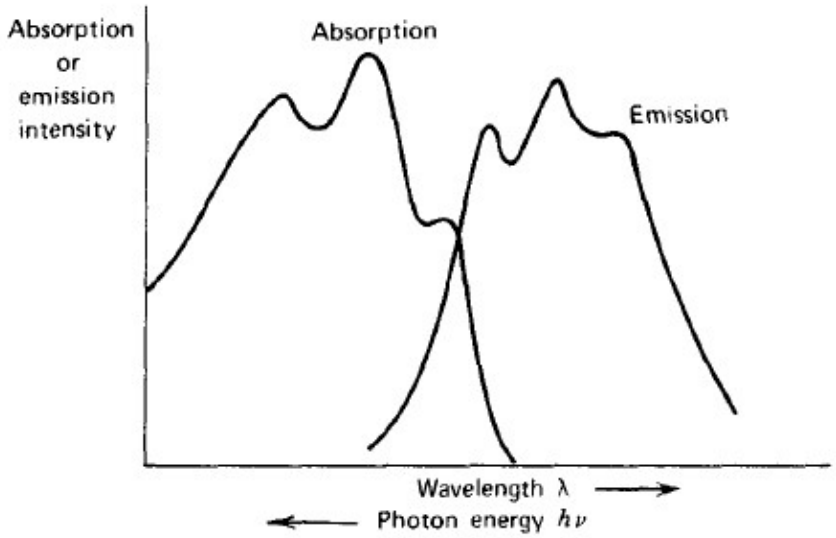

Figure 16: Absorption and Emission Spectra [19]

The wavelength-shifter employed in this investigation, Exalite 416, absorbs the emission photons from PPO at a peak wavelength of 355 nm and re-emits scintillation photons at a peak wavelength of 416 nm, corresponding to a Stokes shift of 61 nm [36] [37]. The peak wavelength of emitted photons is within the peak quantum efficiency range (i.e., $> 20\%$ between $\sim$350-420 nm) of the bialkali photocathode of the PMT that is employed in this investigation, as shown in Figure 17.

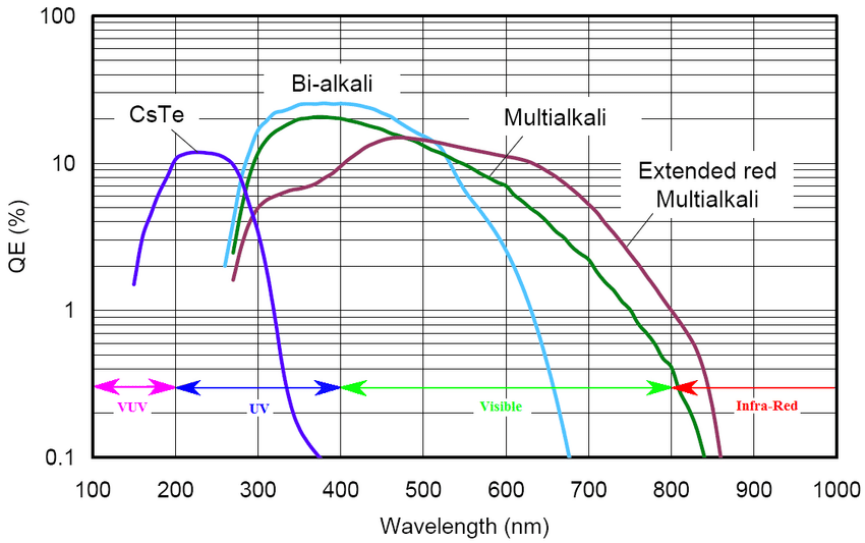

Figure 17: Quantum Efficiency Comparison of Bialkali to Other Photocathodes [38]

2.2.6 Performance Comparison Metrics

Quantitative metrics are utilized to characterize scintillator performance. These metrics facilitate comparison of the novel scintillators to each other and to existing scintillators. The performance metrics utilized in this investigation include relative light yield and relative efficiency.

Light yield (η) is a measure of scintillation photons generated per unit of energy deposited by incident (or recoil) particles and is defined via Equation 7 [39].

$$\eta = \frac{\#\ photons\ generated}{energy\ deposited} \tag{7}$$

As the number of scintillation photons may be difficult to accurately quantify, relative light yield (L_{rel}) may be defined via Equation 8,

$$L_{rel} = \frac{X_{novel\ \ scintillator}}{X_{standard\ \ scintillator}} \tag{8}$$

where $X_{novel\ \ scintillator}$ is the channel corresponding to an energy-spectrum feature of a novel scintillator and $X_{standard\ \ scintillator}$ is the channel corresponding to the analagous

energy-spectrum feature of a scintillator serving as a standard of comparison. In situations where a discernible photopeak is not part of the spectrum, the Compton edge can be used to enable comparisons about relative light yield, as long as measurement conditions are maintained.

Intrinsic efficiency (ε_{int}) is a measure of radiation quanta detected compared to the radiation quanta incident on the detector surface and is defined via Equation 9 [19],

$$\varepsilon_{int} = \frac{\#\ pulses\ recorded}{\#\ radiation\ quanta\ incident\ on\ detector}. \tag{9}$$

Relative efficiency may also be quantified as a ratio of intrinsic efficiency of a novel scintillator to that of a known standard, as in Equation 10 [40],

$$Efficiency_{rel} = \frac{\varepsilon_{int}\ (novel\ scintillator)}{\varepsilon_{int}\ (standard\ scintillator)}. \tag{10}$$

III. Methodology

3.1 Formulation, Curing, and Finishing Procedures

In this research, novel scintillator formulations are produced by varying the relative amounts of constituent materials in ways expected to improve detection performance or structural integrity and unlikely to have an undue negative impact on these parameters. Unfortunately, alterations that result in improvement of one parameter may produce a negative impact on another parameter so this process is often an exercise in optimization. The process begins when relative percentages of constituent materials are determined and then multiplied by the desired mass of the unfinished (i.e., unpolished) scintillator to determine the required masses of the constituent materials. By convention, percentages of all materials, except Exalite 416 and TPO, sum to 100% (thus, total percentages, including Exalite 416 and TPO) will sum to slightly more than 100%). This convention has been adopted in previous investigations for ease of comparison of relative proportions of monomers, crosslinkers, chromophores, fluorophores, and high-Z compounds [1]. Although accuracy is limited by available means of adding liquid components to our formulations, which permits no greater precision than 10^{-2} grams, the slight differences in calculated scintillator mass are on the same order of magnitude or less as compared to the expected measurement error.

The formulations are mixed in borosilicate glass reaction vials with outer dimensions of 28 mm diameter by 57 mm tall, with 1 inch inner diameter. Upon adding the TPO, the vials are wrapped light-tight in aluminum foil and kept out of ambient light as much as possible in order to prevent premature curing. A combination of heating on hotplates and mixing via sonic bath vibration is then conducted until all constituents are dissolved and the resulting scintillator solution is homogeneous (if a fully-dissolved homogeneous solution is achievable). The formulations are then placed

in an inert glovebox (with a N_2 atmosphere and <0.1 ppm O_2), and each scintillator solution is sparged with N_2 gas. The purpose of sparging is to displace any O_2 that may be dissolved in the scintillator solutions as the presence of dissolved O_2 could result in undesirable reactions during the curing process or additional non-radiative quenching pathways. Pressure relief caps are affixed tightly to the reaction vials prior to removal from the glovebox to preserve the inert gas (and absence of significant levels of O_2) inside the reaction vials.

When the scintillator solutions have cooled to room temperature, the curing process commences. Curing is initiated with the Formlabs 'Form Cure' (Figure 18), which uses LED light of 405 nm wavelength at 9.1 W radiant power to cure the scintillators. The curing process is conducted over several iterations of active curing (with segment durations ranging in duration from 1-60 seconds) alternating with cooling cycles (with segments ranging in duration from 10-300 seconds). After the Formlabs procedure is complete and the samples have solidified, the scintillators are again allowed to cool to approximately room temperature. Then, the next stage of curing commences with the Dymax 'BlueWave AX-550 VisiCure' (Figure 19), which uses LED light of 405 nm wavelength at 125 W radiant power. Since the plastic has almost completely cured by the completion of the Formlabs procedure (and, thus, the potential for substantial heat buildup from further curing is significantly diminished), the Dymax procedure can proceed with longer active curing segments (ranging in duration from 30-60 seconds) and much shorter cooling cycles (ranging in duration from 10-60 seconds), notwithstanding its appreciably higher intensity. For all described investigations, active curing time using the Formlabs apparatus ranged from 5-7 minutes and active curing time with the Dymax apparatus ranged from 4-6 minutes. Total cooling times ranged from 12-60 minutes. Longer cooling time segments were often implemented in an effort to reduce the likelihood of scintillator cracking during

the curing process, which is believed to be caused (at least in part) by insufficient heat dissipation.

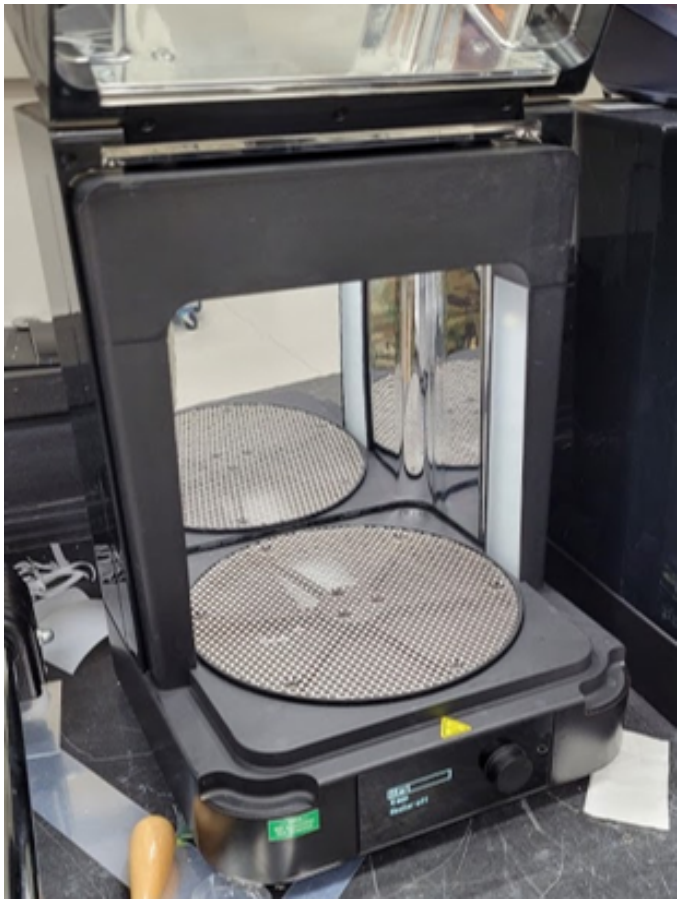

Figure 18: Formlabs Form Cure with lid open, showing the area where the scintillator samples are placed for curing

Upon completion of the curing procedure, the 'finishing stage' is the final step of scintillator preparation. The finishing procedure consists of sanding and polishing the circular faces of the cylindrical scintillators using sandpaper with increasing grit, moving from 400-grit, 1,000-grit, 2,000-grit, and ∼30,000-grit to achieve smooth, clear surfaces. The finishing is conducted in a wet environment and the first three finishing stages are completed using a mixture of water and mild liquid soap. The final finishing stage includes a water and alumina (0.3 μm) slurry. The sanding is conducted by moving the scintillators across the sandpaper surfaces under moderate hand pressure

Figure 19: Dymax BlueWave AX-550 VisiCure with four scintillator samples placed in the curing region

in a figure-eight motion, which is more likely than circular or linear motions to yield a uniformly flat and smooth scintillator face. The sides of the cylincrical scintillators do not require any finishing, as their interface with the inner surface of the cylindrical reaction vials results in a clear surface with proper shape. The upper circular face (with respect to the reaction vial) is characterized by a curved meniscus after curing, which must be finished to a smooth, uniformly flat face for optimal detector performance, since this face will be mounted against the PMT. Of lesser importance is the finishing of the lower circular face, which is characterized by mild contours from the slightly non-flat, inner, bottom surface of the reaction vial. Upon completion of finishing (assuming the samples have not cracked during the curing and finishing

processes), the scintillators are ready for performance evaluation and characterization.

3.2 Prototype Formulation

A novel plastic scintillator formulation was proposed based on an existing, non-high-Z loaded fast-curing design[1]. The key difference was the addition of a high-Z material to enhance photon sensitivity. Triphenyl bismuth ($BiPh_3$) was employed for this purpose in the initial formulation (Bi-Plastic). The formulations for both the previously existing formulation and the initial high-Z-loaded formulation are detailed in Table 2. The percentages listed in Table 2 were multiplied by 10 grams to yield a 10-gram unfinished sample. The same photocuring procedure was employed for both, which took a total of 24 minutes to complete. This process consisted of active curing iterations with 405-nm-wavelength light (i.e, 5 minutes of curing with the FormLabs Form Cure followed by 4 minutes of curing with the Dymax BlueWave AX-550 VisiCure, in segments ranging from 5-60 seconds), alternating with cooling iterations (totaling 15 minutes, in segments ranging from 10-180 seconds).

Table 2: Prototype Scintillator Formulation

Name	**IBOA**	**PPO**	**DIPN**	**HDDMA**	**BPADM**	**TPO**	**E416**	**$BiPh_3$**
AFIT 131	49.0%	15.0%	15.0%	10.5%	10.5%	0.10%	0.20%	00.0%
Bi-Plastic	44.1%	13.5%	13.5%	9.45%	9.45%	0.09%	0.18%	10.0%

3.3 Primary Fluorophore and High-Z Compound Variation Study

The next phase of the investigation explored variation of two parameters: primary fluorophore content and high-Z compound content. Beginning with these investigations, most samples were formuluated with unfinished masses of 18 grams or 15 grams,

in contrast to the 10-gram unfinished mass of the Bi-Plastic scintillator. This greater mass was chosen so that, after finishing, the scintillators would be close to the same dimensions of the commercially available standards of comparison, i.e., approximately 1 inch long by 1 inch diameter cylinders. From this point onward in the investigation, each scintillator sample was assigned a unique designator using the naming convention of "AFIT XXX", where "XXX" is a unique three-digit number.

3.3.1 Common Procedures

Upon addition of all individual scintillator components in the reaction vials, the samples were wrapped in aluminum foil and placed in the digital ultrasonic bath (H&B Luxuries Digital Ultrasonic Cleaner) where they were subjected to 35 kHz vibrations in a water medium for two successive cycles of 480 seconds. The most common use of an ultrasonic bath is cleaning of small objects, but it is employed in this investigation to facilitate mixing of scintillator components. After the ultrasonic bath treatment, the samples were placed on a heat plate set to below the boiling temperature of the solution for whatever duration was required until all components were mixed homogeneously. For some samples, however, the components did not go into solution and these were considered to be failed formulations. For samples in which all components successfully went into solution, the next step was sparging with N_2 in the inert glove box for 15 minutes. After sparging, the vials were re-wrapped in aluminum foil until the start of the curing process. The curing protocol for all samples was a total of five minutes of active curing in the Formlabs Form Cure and four minutes of active cooling in the Dymax BlueWave AX-550 VisiCure. Tables 3 & 4 provide the breakdown of active curing and cooling iterations.

Table 3: Curing Time Protocol (Formlabs): Primary Fluor and High-Z Variation

Iteration	**1**	**2**	**3**	**4**	**5**	**6**	**7**
Curing Duration [s]	10	10	10	30	60	90	90
Cooling Duration [s]	60	60	60	120	180	180	-

Table 4: Curing Time Protocol (Dymax): Primary Fluor and High-Z Variation

Iteration	**1**	**2**	**3**	**4**	**5**	**6**	**7**	**8**
Curing Duration [s]	30	30	30	30	30	30	30	30
Cooling Duration [s]	10	10	10	10	10	10	10	-

3.3.2 AFIT 001

AFIT 001 was formulated in an attempt to replicate the Bi-Plastic prototype with an unfinished mass of 18 grams. The formulation is provided in Table 5.

Table 5: AFIT 001 Formulation

	IBOA	**PPO**	**DIPN**	**HDDMA**	**BPADM**	**TPO**	**E416**	**$BiPh_3$**
Proportion	44.1%	13.5%	13.5%	9.45%	9.45%	0.09%	0.09%	10.0%
Mass [g]	7.9380	2.4300	2.4300	1.7010	1.7010	0.0162	0.0324	1.8000

3.3.3 AFIT 002

AFIT 002 was formulated in an attempt to produce a sample similar to the Bi-Plastic prototype with an 18-gram unfinished mass. The key difference with AFIT 002 is that the PPO content is doubled (entirely replacing the DIPN content). The formulation is given in Table 6.

Table 6: AFIT 002 Formulation

	IBOA	**PPO**	**DIPN**	**HDDMA**	**BPADM**	**TPO**	**E416**	**$BiPh_3$**
Proportion	44.1%	27.0%	0.0%	9.45%	9.45%	0.09%	0.09%	10.0%
Mass [g]	7.9380	4.8600	0.0000	1.7010	1.7010	0.0162	0.0324	1.8000

3.3.4 AFIT 003, AFIT 004, & AFIT 005

AFIT 003, AFIT 004, and AFIT 005 were formulated nearly simultaneously, paying special attention to abide by sterile lab practices, as it was suspected that unidentified contaminants were responsible for the cloudy consistencies of AFIT 001 and AFIT 002, shown in Chapter IV. The AFIT 003 formulation is identical to the AFIT 002 formulation, while the AFIT 004 formulation is similar to the AFIT 003 formulation but with 5 wt% greater $BiPh_3$ content and 5 wt% less PPO content. The AFIT 005 formulation also mirrors the AFIT 003 formulation but with 10 wt% greater $BiPh_3$ content and 10 wt% less PPO content. All samples were formulated with unfinished masses of 18 grams. The formulations are listed in Tables 7, 8, & 9.

Table 7: AFIT 003 Formulation

	IBOA	**PPO**	**DIPN**	**HDDMA**	**BPADM**	**TPO**	**E416**	**$BiPh_3$**
Proportion	44.1%	27.0%	0.0%	9.45%	9.45%	0.09%	0.09%	10.0%
Mass [g]	7.9380	4.8600	0.0000	1.7010	1.7010	0.0162	0.0324	1.8000

Table 8: AFIT 004 Formulation

	IBOA	**PPO**	**DIPN**	**HDDMA**	**BPADM**	**TPO**	**E416**	**$BiPh_3$**
Proportion	44.1%	22.0%	0.0%	9.45%	9.45%	0.09%	0.09%	15.0%
Mass [g]	7.9380	3.9600	0.0000	1.7010	1.7010	0.0162	0.0324	2.7000

Table 9: AFIT 005 Formulation

	IBOA	**PPO**	**DIPN**	**HDDMA**	**BPADM**	**TPO**	**E416**	**$BiPh_3$**
Proportion	44.1%	17.0%	0.0%	9.45%	9.45%	0.09%	0.09%	20.0%
Mass [g]	7.9380	3.0600	0.0000	1.7010	1.7010	0.0162	0.0324	3.6000

3.3.5 Impurity Identification, $BiPh_3$ Recrystallization, & AFIT 006

The significant (and consistent) clouding of AFIT 001 - AFIT 005, as shown in Chapter IV, suggested that perhaps it was not an external contaminant but a common impure ingredient causing the fouled appearance. The new supply of $BiPh_3$ was isolated as the likely culprit. To test this theory, one gram of the raw $BiPh_3$ was subjected to a recrystallization procedure. The procedure entailed dissolving the $BiPh_3$ with pure ethanol in a test tube and heating the solution to 70-75°C (below the boiling point of ethanol of 78°C) until the $BiPh_3$ was completely dissolved. Impurities separated out of solution in the form of a yellowish liquid phase below the clear, colorless part of the solution. The impurities were, to the greatest extent possible, siphoned out of the bottom of the solution and the heat continued to be applied until almost all of the ethanol had evaporated. The solution was then placed in a vacuum chamber to completely evaporate the remaining ethanol. The recrystallized $BiPh_3$ appeared as bright, white flaky crystals, in contrast to the raw $BiPh_3$, which appeared as a white powder. A yield of 0.4733 grams of purified $BiPh_3$ was recovered from the recrystallization process. To test the viability of the recrystallized $BiPh_3$, it was used in the formulation of AFIT 006, which was identical to the AFIT 001 formulation with an unfinished mass of approximately 4.75 grams. The formulation is given in Table 10.

The new supply of $BiPh_3$ was of the same grade of purity and from the same manufacturer as the original supply which was used in the formulation for the prototype Bi-Plastic scintillator. The original raw (i.e., unpurified) supply had the appearance

Table 10: AFIT 006 Formulation

	IBOA	**PPO**	**DIPN**	**HDDMA**	**BPADM**	**TPO**	**E416**	**$BiPh_3$**
Proportion	44.1%	27.0%	0.0%	9.45%	9.45%	0.09%	0.09%	10.0%
Mass [g]	2.0873	0.6390	0.6390	0.4473	0.4473	0.0043	0.0085	0.4733

and consistency of bright white flaky crystals, which was characteristic of the new supply only after recrystallization. The appearance and consistency of the new supply, prior to recrystallization, was a whitish powder.

3.3.6 AFIT 007, AFIT 008, & AFIT 009

The constituent profile of AFIT 007 was identical to that of AFIT 002 and AFIT 003, AFIT 008 was identical to AFIT 004, and AFIT 009 was identical to AFIT 005, with the only differences being that recrystallized instead of raw $BiPh_3$ was used and the new formulations would have an unfinished mass of 15 grams. The formulations are provided in Tables 11, 12, & 13.

Table 11: AFIT 007 Formulation

	IBOA	**PPO**	**DIPN**	**HDDMA**	**BPADM**	**TPO**	**E416**	**$BiPh_3$**
Proportion	44.1%	27.0%	0.0%	9.45%	9.45%	0.09%	0.09%	10.0%
Mass [g]	6.6150	4.0500	0.0000	1.4175	1.4175	0.0135	0.0270	1.5000

Table 12: AFIT 008 Formulation

	IBOA	**PPO**	**DIPN**	**HDDMA**	**BPADM**	**TPO**	**E416**	**$BiPh_3$**
Proportion	44.1%	22.0%	0.0%	9.45%	9.45%	0.09%	0.09%	15.0%
Mass [g]	6.6150	3.3000	0.0000	1.4175	1.4175	0.0135	0.0270	2.2500

Table 13: AFIT 009 Formulation

	IBOA	**PPO**	**DIPN**	**HDDMA**	**BPADM**	**TPO**	**E416**	**$BiPh_3$**
Proportion	44.1%	17.0%	0.0%	9.45%	9.45%	0.09%	0.09%	20.0%
Mass [g]	6.6150	2.5500	0.0000	1.4175	1.4175	0.0135	0.0270	3.0000

3.3.7 Gadolinium(III) Oxide Doping: AFIT 041 & AFIT 042

Formulations were attempted using gadolinium(III) oxide as the high-Z compound. These formulations were attempted based on reported successful use of this compound is PS- and PVT-based formulations [3]. The literature did specify, however, that this compound had been used successfully when added to plastic scintillator formulations in the form of nanoparticles (i.e., particles $\leq$100 nm in size). Due to administrative restrictions, nanoparticles were not permitted for use in the available laboratories, so non-nanoized (i.e., particle size >100 nm) were used instead. The AFIT 041 and AFIT 042 formulations were similar to that of AFIT 001 and AFIT 002, respectively, exchanging $BiPh_3$ for Gd_2O_3. AFIT 041 and AFIT 042 were formulated with unfinished masses of 10 grams. The formulations are given in Tables 14 & 15.

Table 14: AFIT 041

Name	**IBOA**	**PPO**	**DIPN**	**HDDMA**	**BPADM**	**TPO**	**E416**	**Gd_2O_3**
Proportion	44.1%	13.5%	13.5%	9.45%	9.45%	0.09%	0.18%	10.0%
Mass [g]	4.41	1.35	1.35	0.945	0.945	0.009	0.018	1.00

Table 15: AFIT 042

Name	**IBOA**	**PPO**	**DIPN**	**HDDMA**	**BPADM**	**TPO**	**E416**	**Gd_2O_3**
Proportion	44.1%	13.5%	13.5%	9.45%	9.45%	0.09%	0.18%	10.0%
Mass [g]	4.41	2.70	0.00	0.945	0.945	0.009	0.018	1.00

3.4 Photoinitiator and Curing Variation Study

Based upon previous work, questions emerged regarding the effects of curing factors on the physical attributes and detection performance of the scintillators. A study was designed to vary the amount of photoinitiator (i.e., TPO) and the curing time protocol. Twelve scintillator designs were proposed. TPO content would be varied at four different levels, i.e., 0.01% (AFIT 100-series), 0.05% (AFIT 101-series), 0.10% (AFIT 102-series), and 0.20% (AFIT 103-series). For each of these series, three identical sets would be produced, and each set would undergo one of three curing time protocols. The three curing time protocols are Protocol A (5 minutes Formlabs + 4 minutes Dymax), Protocol B (7 minutes Formlabs + 6 minutes Dymax), and Protocol C (5 minutes Formlabs + 6 minutes Dymax). Note that these specified curing times represent total "active curing" durations and do not include interspersed cooling cycles. The scintillator formulations are provided in Table 16 and the detailed curing time protocols are provided in Tables 17, 18, 19, 20, 21, & 22.

Table 16: Scintillator Formulations - TPO & Curing Time Study

Name	**IBOA**	**DIPN**	**PPO**	**HDDMA**	**BPADM**	**E416**	**TPO**	**$BiPh_3$**
AFIT100	46.55%	00.00%	28.50%	9.975%	9.975%	0.190%	0.0095%	5.000%
AFIT101	46.55%	00.00%	28.50%	9.975%	9.975%	0.190%	0.0475%	5.000%
AFIT102	46.55%	00.00%	28.50%	9.975%	9.975%	0.190%	0.0950%	5.000%
AFIT103	46.55%	00.00%	28.50%	9.975%	9.975%	0.190%	0.1900%	5.000%

Table 17: Curing Time Protocol A (Formlabs): TPO and Curing Time Study

Iteration	**1**	**2**	**3**	**4**	**5**	**6**	**7**	**8**	**9**	**10**	**11**	**12**	**13**	**14**	**15**
Curing Time [s]	1	1	1	1	1	1	1	1	1	1	1	1	1	1	1
Cooling Time [s]	10	10	10	10	10	10	10	10	10	10	10	10	10	10	10
Iteration	**16**	**17**	**18**	**19**	**20**	**21**	**22**	**23**	**24**	**25**	**26**	**27**	**28**	**29**	
Curing Time [s]	5	5	5	5	5	5	10	10	10	15	15	15	30	30	
Cooling Time [s]	180	180	120	120	60	60	60	120	120	120	120	120	120		

Table 18: Curing Time Protocol A (Dymax): TPO and Curing Time Study

Iteration	**1**	**2**	**3**	**4**
Curing Time [s]	60	60	60	60
Cooling Time [s]	10	10	10	

Table 19: Curing Time Protocol B (Formlabs): TPO and Curing Time Study

Iteration	**1**	**2**	**3**	**4**	**5**	**6**	**7**	**8**	**9**	**10**	**11**	**12**	**13**	**14**	**15**	**16**	**17**
Curing Time [s]	1	1	1	1	1	1	1	1	1	1	1	1	1	1	1	5	5
Cooling Time [s]	10	10	10	10	10	10	10	10	10	10	10	10	10	10	10	180	180
Iteration	**18**	**19**	**20**	**21**	**22**	**23**	**24**	**25**	**26**	**27**	**28**	**29**	**30**	**31**	**32**	**33**	
Curing Time [s]	5	5	5	5	10	10	10	15	15	15	30	30	60	60	60	60	
Cooling Time [s]	180	180	180	120	120	120	120	120	120	120	120	120	120	120	120		

Table 20: Curing Time Protocol B (Dymax): TPO and Curing Time Study

Iteration	**1**	**2**	**3**	**4**	**5**	**6**
Curing Time [s]	60	60	60	60	60	60
Cooling Time [s]	10	10	10	10	10	-

Table 21: Curing Time Protocol C (Formlabs): TPO and Curing Time Study

Iteration	**1**	**2**	**3**	**4**	**5**	**6**	**7**	**8**	**9**	**10**	**11**	**12**	**13**	**14**	**15**	**16**	**17**
Curing Time [s]	1	1	1	1	1	1	1	1	1	1	1	1	1	1	1	5	5
Cooling Time [s]	10	10	10	10	10	10	10	10	10	10	10	10	10	10	180	300	300
Iteration	**18**	**19**	**20**	**21**	**22**	**23**	**24**	**25**	**26**	**27**	**28**	**29**	**30**	**31**	**32**	**33**	
Curing Time [s]	5	5	5	5	10	10	10	15	15	15	30	30	30	30	30	30	
Cooling Time [s]	240	240	180	180	180	180	180	180	180	180	120	120	120	120	120		

Table 22: Curing Time Protocol C (Dymax): TPO and Curing Time Study

Iteration	**1**	**2**	**3**	**4**	**5**	**6**
Curing Time [s]	60	60	60	60	60	60
Cooling Time [s]	10	10	10	10	10	

The common procedures detailed in Section 3.3.1 regarding wrapping in foil, mixing, heating, sparging, and preparing for curing were followed for the scintillators in this part of the investigation. All proposed scintillator formulations for the TPO and curing time study produced homogeneous solutions prior to curing. All scintillators had the same high-Z loading of 5 wt% $BiPh_3$ and all were formulated to have an unfinished mass of 15 grams.

3.5 Experimental Procedures

Relative scintillator performance is evaluated by measuring the detection response of each using consistent radioactive sources, equipment, and methods. Each scintillator is first prepared by wrapping two layers of one-inch wide, white polytetrafluoroethylene (PTFE) tape (specification: Mil-T-27730A, A-A-58092) around all surfaces except the one that interfaces with the borosilicate glass window of the PMT. For all measurements discussed herein, the PMT employed was a Hamamatsu R7724 PMT [41]. The unwrapped scintillator face in contact with the PMT window is coated with a thin layer of Saint-Gobain Crystals BC-630 silicone grease to ensure continuity of transparent media with similar indices of refraction. The scintillator is then affixed to the PMT window, with the silicone grease providing moderate adhesion, and capped by an aluminum fitting with a rubber gasket for a light-tight fit, as shown in Figure 20 in the standard detection setup.

Source measurements were conducted using ^{57}Co and ^{137}Cs gamma sources. Source characteristics, including current activities (as of 01 January 2022) are provided in Table 23. The ^{137}Cs source was placed in direct contact with the detector and the ^{57}Co gamma source was placed with a standoff of two inches from the detector. These distances were empirically determined to provide optimal counting statistics with minimal pileup events and detector saturation. Source detections were collected

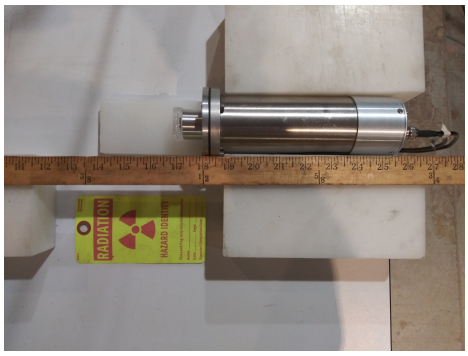

(a) Detection Setup (Top)

(b) Detection Setup (Front)

Figure 20: Standard Detection Setup

with each scintillator for 300 seconds. Detector outputs were recorded via a CAEN DT5730 digitizer and the PMT was powered by a CAEN DT5533E HV power supply module at -1,500 V bias voltage, with CoMPASS data acquisition software and GECO voltage control software providing the operational interface [42, 43, 44, 45].

Table 23: Radioactive Sources Used for Scintillator Characterization

Nuclide	**Half-Life (days)**	**Calibration Activity (μCi)**	**Calibration Date**	**Time Since Calibration (days)**	**Current Activity (μCi)**
^{57}Co	271.78	10.10	15 Feb 2019	1,051	0.6922
^{137}Cs	10,983.07	10.00	01 Sep 2000	7,792	6.1155

As much as possible, the scintillators in this investigation were fabricated to yield finished products that are equivalent in size and shape. The finished scintillators are all right circular cylinders of 1 inch in diameter and approximately one inch in length, but it is not uncommon for the lengths to vary by +/- 0.1 inch. Collections with sources are made under identical environmental conditions, as much as is practicable. The equipment settings are held constant for equivalent characterizations with sources, unless otherwise noted. Maintaining consistent distances, solid angles, and other experimental parameters permits comparative performance analysis of the novel scintillators.

3.6 Evaluation of Physical Characteristics and Performance Metrics

The primary physical characteristics by which the scintillators are evaluated include hardness, temporary coloring, leaching, and propensity to crack during the curing process. Hardness is quantitatively evaluated via the Shore A durometer test. Shore durometers determine hardness by measuring the penetration depth of a probe on a 0-100 scale. The Shore A durometer utilizes a blunt probe and the Shore D durometer utilizes a sharp probe, as seen in Figure 21. This investigation employed the Shore A durometer shown in Figure 22. Measurements of hardness with the Shore A durometer were taken for scintillators that were finished and intact, even if cracking or surface fissuring had occurred.

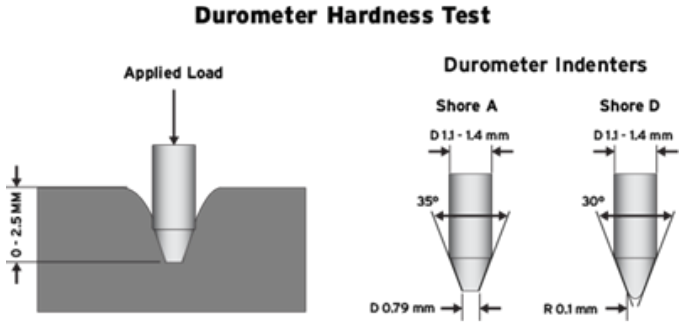

Figure 21: Measuring hardness with Shore A and Shore D durometers [2]

Temporary purple coloring is commonly observed immediately following the curing process and the extent appears to be correlated with PPO concentration. Coloring is evaluated qualitatively by observation while the quantitative effects of coloring are determined from a measure of relative light yield in comparison to scintillators that have undergone no (or less) coloring upon curing.

PPO leaching, which produces a hazy film on the surface of the scintillators, is observed with some scintillator formulations and appears to be correlated with higher PPO content. Leaching is not typically observed in scintillator formulations with 15 wt% or less PPO but is common among scintillators formulated with 20-30 wt%

Figure 22: The Shore A durometer employed in this investigation

PPO [1]. Treatment with ethanol has been shown in previous studies to prevent or significantly reduce the occurrence of leaching, with material loss of only 0.20-0.37 wt% [1] [46]. In this investigation, ethanol treatment was administered 68 days after curing via immersion of the scintillators in 70 vol% denatured ethanol for a duration of one hour.

Cracking of novel scintillators during the curing process is not an uncommon occurrence and is likely due to insufficient heat dissipation. Previous attempts to remedy this issue with more frequent and longer duration cooling iterations during the curing process have been only partially successful. One option explored in the primary investigation to mitigate cracking was to vary the concentration of the photoinitiator (i.e., TPO). The photoinitiator concentration affects the rate and extent of curing. A minimum concentration of photoinitiator is necessary to fully cure the scintillator, but too much can result in rates of curing that rapidly generate large amounts of heat, which is believed to contribute to sample cracking. Therefore, an

optimal photoinitiator concentration must exist between these two extremes. These factors, along with the observation that fluorescent light yield of plastic scintillators increases with greater curing time (from 0 to 540 seconds), motivated the primary investigation of altering TPO concentration and curing time to explore the effects on the scintillators' physical attributes and performance characteristics.

The relative light yield determinations are made by recording the uncalibrated energy histograms of standard scintillators (i.e., EJ-256) and comparing them to the energy histograms of the novel scintillators. The ADC channels corresponding to analogous spectrum features provide a relative comparison of light yield, as calculated via Equation 8. For the ^{57}Co spectra, the channel corresponding to the centroid of the photopeak is used to determine the relative comparison. For the ^{137}Cs spectra, the channel corresponding the Compton edge is used, where the Compton edge is approximated by the inflection point of the fitted Gaussian curve.

The relative efficiency determinations are made similarly, by calculating the detection efficiency of standard scintillators for specific spectrum features. Estimation of intrinsic efficiency is accomplished by determining counts in the energy histograms beyond the centroid of the photopeak as a proportion of total counts for the ^{57}Co spectra. An similar method is used to approximate intrinsic efficiency from the ^{137}Cs spectra, using the proportion of counts beyond the estimated Compton edge as the comparison value. Since the source collection parameters are held fixed, the number of radiation particles incident on the detector face should be very close to equal for all collections. Thus, the relative efficiency calculation, given by Equation 10, is simply a ratio of the number of events recorded by the novel scintillator to the standard scintillator.

IV. Results and Analysis

4.1 Prototype Bismuth-Loaded Scintillator

The prototype bismuth loaded scintillator (Bi-Plastic) is characterized by remarkable optical clarity and a slight yellow coloring as compared to the AFIT 131 standard formulation scintillator which was fabricated simultaneously. The Bi-Plastic is of sufficient hardness to not deform under manual pressure and was able to endure the finishing process with no cracking or deformation. The slight purple coloring that occurred subsequent to the curing process faded within a few days. There has been no noticeable leaching, likely due to the relatively low PPO content of 13.5 wt%. The Bi-Plastic scintillator did not crack during the curing process. An image of the Bi-Plastic scintillator, alongside its corresponding formulation without $BiPh_3$, is shown in Figure 23. A slight yellowing of the prototype scintillator (on the right) occurred in comparison to the unloaded scintillator (on the left).

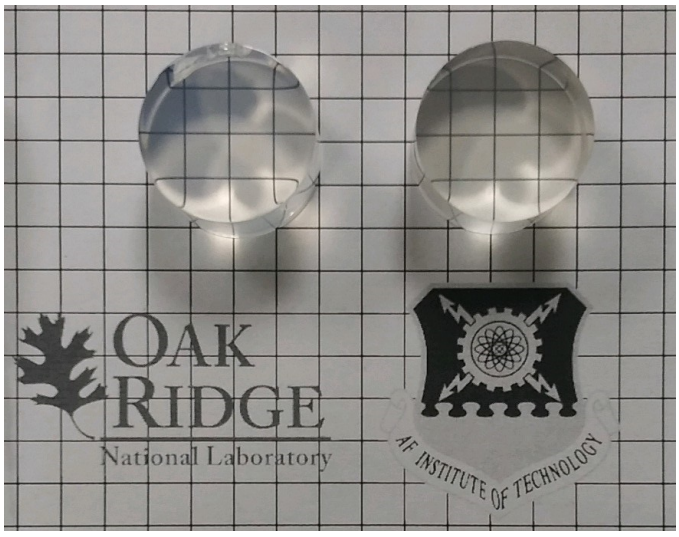

Figure 23: Scintillator without bismuth loading (left) and prototype Bi-Plastic scintillator (right)

The Bi-Plastic scintillator performance was measured with a ^{137}Cs gamma source.

The energy histogram from the ^{137}Cs (which has a signature gamma emission at 662 keV) does not yield a discernible photopeak but the spectrum does exhibit a possible "full energy feature" in the form of a "tail" that is not characteristic of a Gaussian-shaped Compton edge. The energy histograms for AFIT 131 and the Bi-Plastic prototype are seen in Figure 24. This tail feature exhibited by the Bi-Plastic prototype extended into the channel region where a photopeak, or a K_α escape peak at $\sim$80 keV less, would be expected. The spectra demsonstrate that the light yield of the Bi-Plastic scintillator is only approximately 40% that of AFIT 131, but the efficiency is shown to increase over the unloaded sample by a factor of approximately 170%.

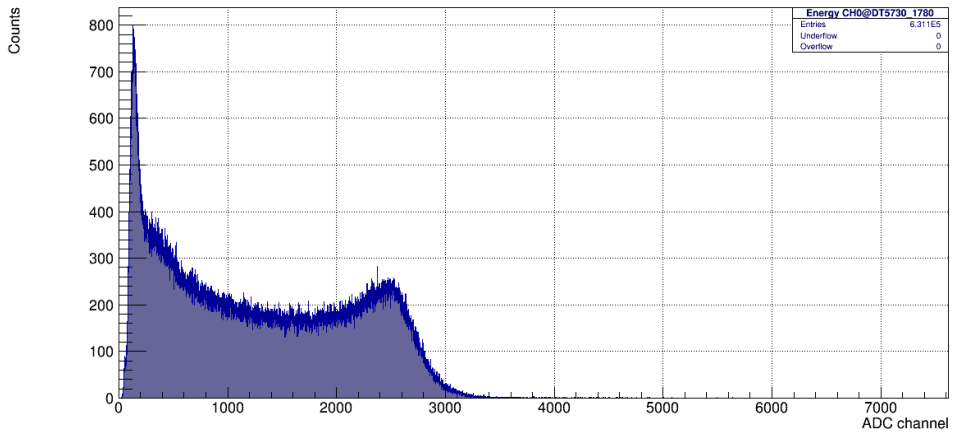

(a) AFIT 131

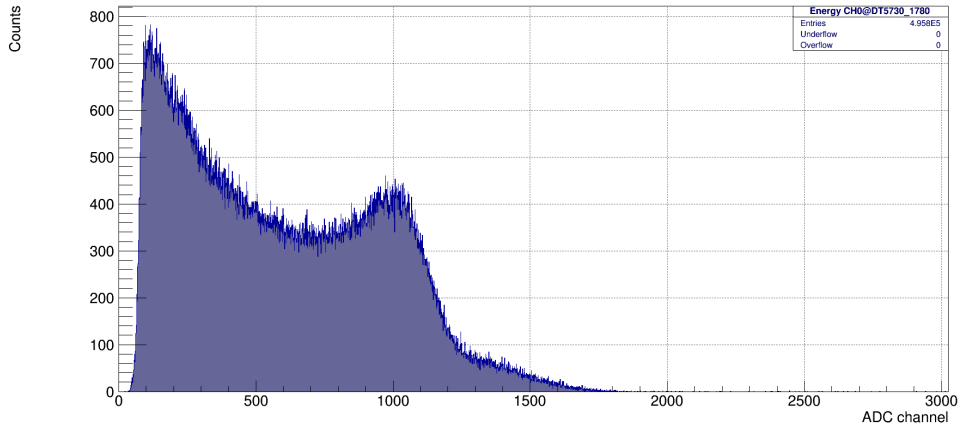

(b) Bi-Plastic

Figure 24: AFIT 131 & Bi-Plastic Scintillator - ^{137}Cs Energy Histogram Comparison

From comparison of the spectra in Figure 24, it can be seen (by absence of a photopeak) that few full-energy depositions of high-energy incident photons occur in the scintillator, where "high-energy" is loosely defined as >500 keV. This is likely due in part to the small mass (∼10 g) of the scintillator sample. For this reason, additional gamma sources were selected for future characterizations in an effort to determine if full-energy deposition is possible for the Bi-Plastic scintillator at lower-energy radiation regimes. The nuclide ^{57}Co (with photopeak at 122 keV) was employed for scintillator characterization and yielded modest photopeak generation in subsequent scintillator samples.

4.2 Primary Fluorophore and High-Z Compound Variation Study

4.2.1 AFIT 001 - AFIT 005

Upon curing, AFIT 001 exhibited a yellowish tinge and was very cloudy. AFIT 002 had a yellowish tinge (slightly less yellow than AFIT 001) and was also very cloudy. AFIT 003 had a yellowish tinge (very similar to AFIT 002), was very cloudy, and cracked after the completion of the Formlabs curing procedure. These samples can be seen in Figure 25.

(a) AFIT 001 (b) AFIT 002 (c) AFIT 003

Figure 25: Initial Samples Exhibiting Significant Cloudiness

The components of AFIT 004 and AFIT 005 did not go into solution upon mixing and heating and, thus, were not cured. AFIT 004 and AFIT 005 are the two vials on the left in Figure 26. Due to excessive cloudienss, cracking, or failure of components to go into solution, AFIT 001 - AFIT 005 were not characterized with sources.

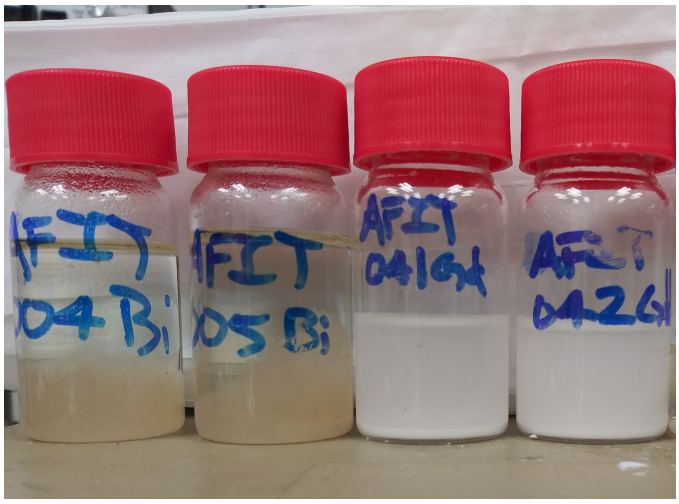

Figure 26: AFIT 004, AFIT 005, AFIT 041, & AFIT 042

4.2.2 Impurity Identification, $BiPh_3$ Recrystallization, & AFIT 006

Upon curing, AFIT 006 had a remarkably clear and colorless appearance, in stark contrast to AFIT 001 - AFIT 005, as seen in Figure 27a. Due to the success of the pilot recrystallization process, the same procedure was followed but scaled up with a starting mass of 25 grams of raw $BiPh_3$. The impure liquid phase can be seen settling at the bottom of the beaker in Figure 27b as the $BiPh_3$ and ethanol solution is heated. The recovered yield was approximately 16.6 grams, or 66%.

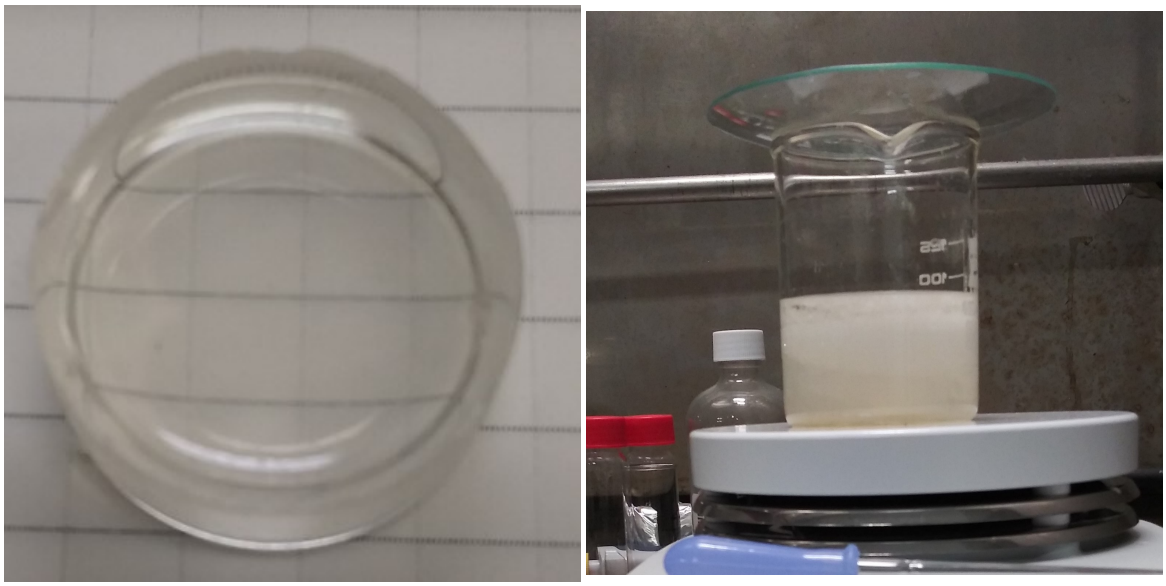

(a) AFIT 006 (b) Recrystallization of $BiPh_3$

Figure 27: Marked Improvement of Scintillator Clarity (a) From $BiPh_3$ Recrystallization (b)

4.2.3 AFIT 007 - AFIT 009

AFIT 007 (10 wt% $BiPh_3$), AFIT 008 (15 wt% $BiPh_3$), and AFIT 009 (20 wt% $BiPh_3$) all cured with a slightly yellowish tinge but appeared remarkably clear compared to formulations with unpurified $BiPh_3$, as can be seen in Figure 28. AFIT 009 cracked after two minutes of curing with the Formlabs Form Cure.

(a) AFIT 007 (b) AFIT 008 (c) AFIT 009

Figure 28: Varying High-Z Content Scintillators

AFIT 007 and AFIT 008 were characterized in terms of relative light yield and sensitivity using ^{137}Cs and ^{57}Co gamma sources. Similar to the earlier energy histogram of the Bi-Plastic scintillator with the ^{137}Cs gamma source, no discernible photopeak exists for AFIT 007 and AFIT 008 but the extended feature beyond the Compton edge is evident for these samples as well as for the EJ-256 spectrum, as evident in Figure 29. These scintillators do, however, exhibit modest photopeaks with a ^{57}Co source, similar to those exhibited by the EJ-256 (5 wt% lead-loaded) standard (Figure 30) and an experimental 8 wt% Bi formulation from a separate study (Figure 31) [3]. It should be noted that the scintillator used to create the ^{57}Co spectrum in Figure 31 was of much larger volume (14 in^3) than the scintillators in this study ($\sim$0.8 in^3). Regarding the ^{57}Co spectra, the Compton edge (at $\sim$39 keV) closely coincides with the K_α escape peak for bismuth (at $\sim$ 45 keV), which can obscure these features and render conclusions less certain. Table 24 provides relative metrics of measured light yield and efficiency as compared to EJ-256.

Table 24: Performance Metrics of AFIT 007 & AFIT 008 Compared to EJ-256

	^{137}Cs		^{57}Co	
	007	008	007	008
Light Yield	0.42	0.27	0.41	0.27
Efficiency	2.25	3.12	2.10	4.43

These results support previous and well-established findings that higher-Z loading leads to increasingly depressed light yields and higher photon sensitivities. These outcomes informed the subsequent study (varying photoinitiator content and curing time) by indicating that scintillators with lower concentrations of bismuth could potentially achieve useful photon sensitivity levels while facilitating greater light yield. These findings further reveal that fast-curing scintillators can be fabricated and function as intended at high-Z loadings of this level.

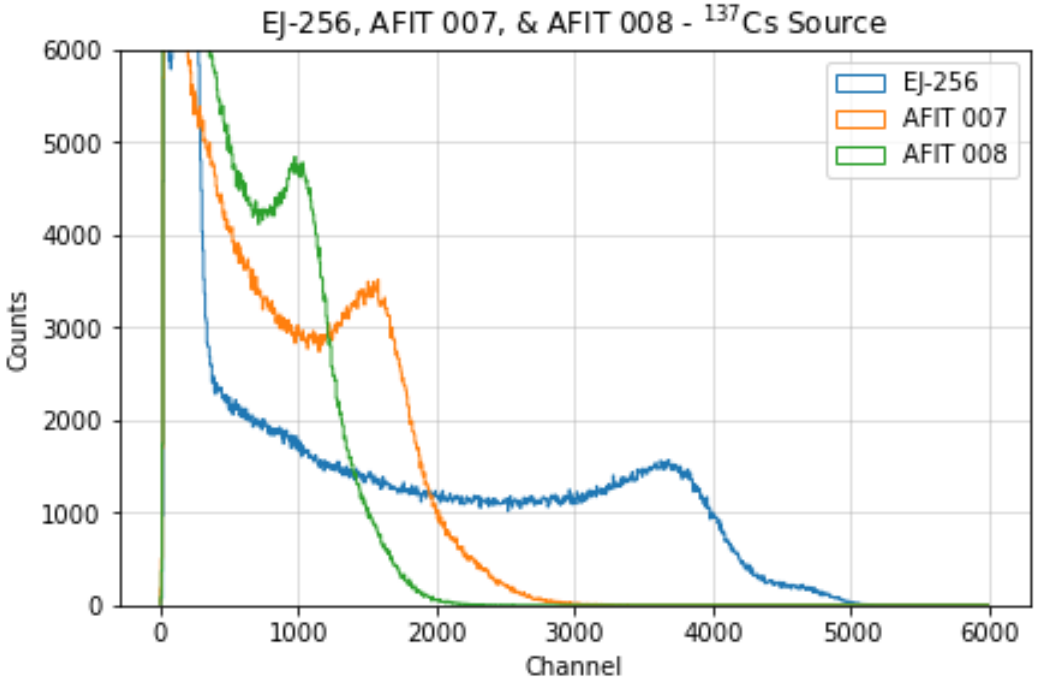

Figure 29: EJ-256, AFIT 007, & AFIT 008 Energy Spectra with ^{137}Cs Source

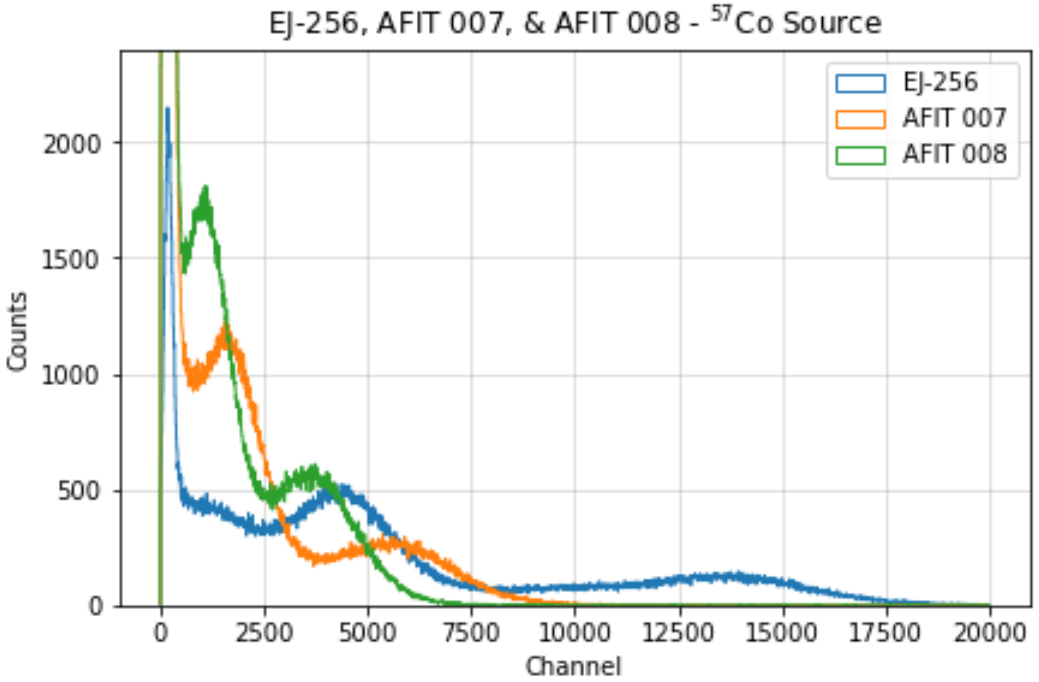

Figure 30: EJ-256, AFIT 007, & AFIT 008 Energy Spectra with ^{57}Co Source

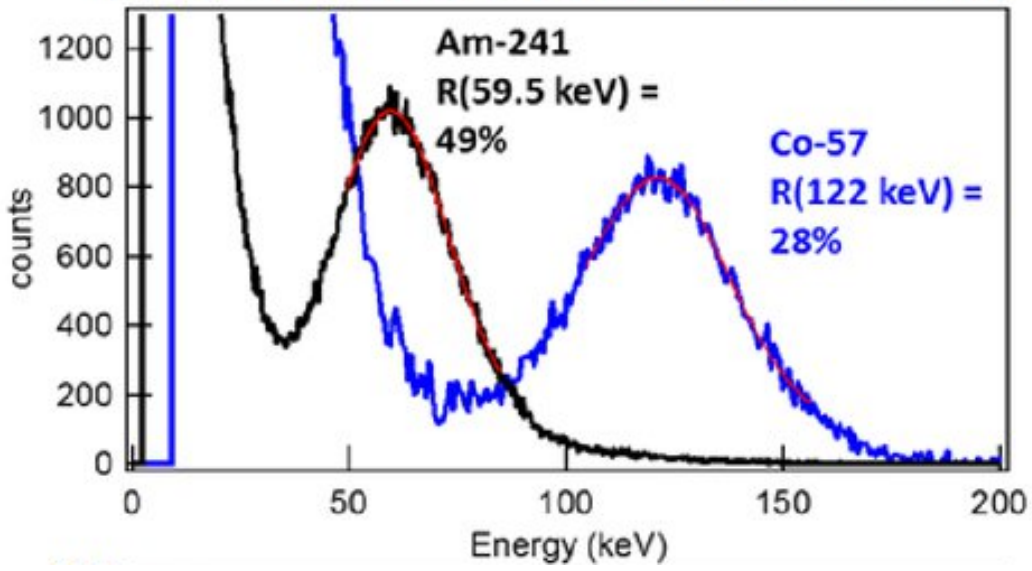

Figure 31: Energy spectra of experimental 14 in^3, 8 wt% Bismuth-Loaded Scintillator [3]

4.2.4 Gadolinium(III) Oxide Doping: AFIT 041 & AFIT 042

The constituent components of these formulations did not go into solution, as seen in the two vials on the right in Figure 26, likely due to the presence of the non-nanoized Gd_2O_3. Consequently, no experimental data were measurable from the AFIT 041 and AFIT 042 samples.

4.3 Photoinitiator and Curing Variation Study

4.3.1 Effects of Curing

Immediately upon curing, key trends emerged. Specifically, the photoinitiator concentration was found to be highly correlated with the degree of "purpling" observable within the samples, with higher concentrations corresponding to deeper coloring, as seen in Figure 32. This purple coloring, however, faded rapidly in most samples, but it did not fade completely in all samples. At 60 days post-cure, the 100- and 101-series scintillators showed no discernible purpling to the naked eye, but the 102-

and 103-series continued to exhibit residual purpling. Furthermore, none of the 100- or 101-series scintillators cracked during the curing procedure; however, four out of six of the 102- and 103-series scintillators cracked, specifically one from Protocol A (nine minutes total active cure time), two from Protocol B (13 minutes total active cure time), and one from Protocol C (11 minutes total active cure time).

Figure 32: (top to bottom) AFIT 100A (0.01 wt% TPO), AFIT 101A (0.05 wt% TPO), AFIT 102A (0.10 wt% TPO), & AFIT 103A (0.20 wt% TPO) immediately after curing

All novel scintillators exhibited appreciable leaching on the surface, which was expected due to the high PPO content of 28.5 wt%. At 68 days post cure, the ethanol treatment detailed in Section 3.6 was performed, which resulted in significantly improved and enduring surface clarity.

Additionally, photoinitiator (i.e., TPO) concentration was found to significantly affect whether the samples cracked during curing. Of the formulations with 0.01 wt% or 0.05 wt%, none of the total of six scintillators cracked. Of the formulations with

0.10 wt% (which was the standard used in previous formulations), two out of three cracked. Similarly, of the formulations with 0.20 wt%, two out of three cracked. The scintillators formulated with 0.01 wt% TPO were the most clear and colorless upon curing, but all of these samples developed exetensive surface fissuring in the weeks after curing. The relative clarity and surface fissuring of the 100-series scintillators can be seen in Figure 33.

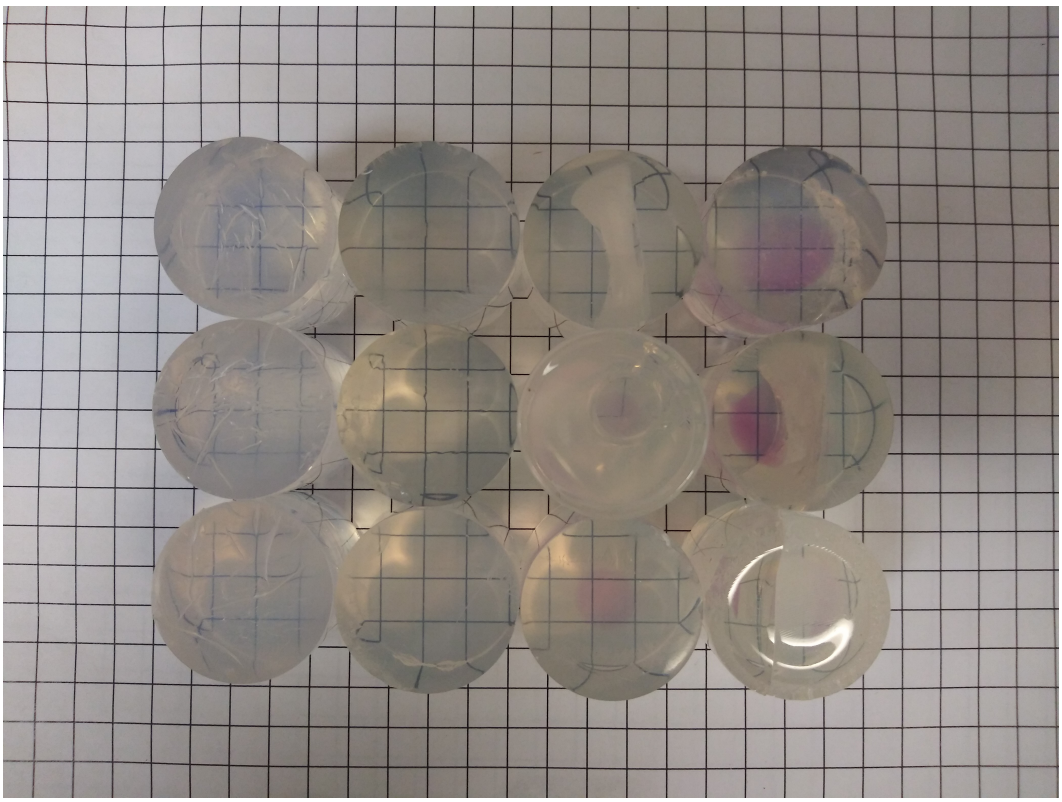

Figure 33: Clarity, Color, and Surface Feature Comparison of
(Top Row) AFIT 100A, 101A, 102A, 103A
(Middle Row) AFIT 100B, 101B, 102B, 103B
(Bottom Row) AFIT 100C, 101C, 102C, 103C

4.3.2 Spectral Analysis

As is evident from the following energy histogram spectra, characterization of the scintillators with the ^{137}Cs gamma source revealed no discernible photopeaks but an

extended feature beyond the Compton edge is apparent. The spectra also reveal that the scintillators do exhibit a modest photopeak with a ^{57}Co source. Spectra of the scintillators are grouped by photoinitiator content and by curing time protocol and are displayed with the EJ-256 spectrum for comparison. Relative light yield and efficiency are also determined with respect to EJ-256.

The energy histogram spectra measured using the AFIT A-series scintillators (i.e., AFIT 100A, AFIT 101A, and AFIT 103A) with separate ^{137}Cs and ^{57}Co sources are provided in Figures 34 and 35, respectively. AFIT 102A performance was not characterized due to cracking during the curing process.

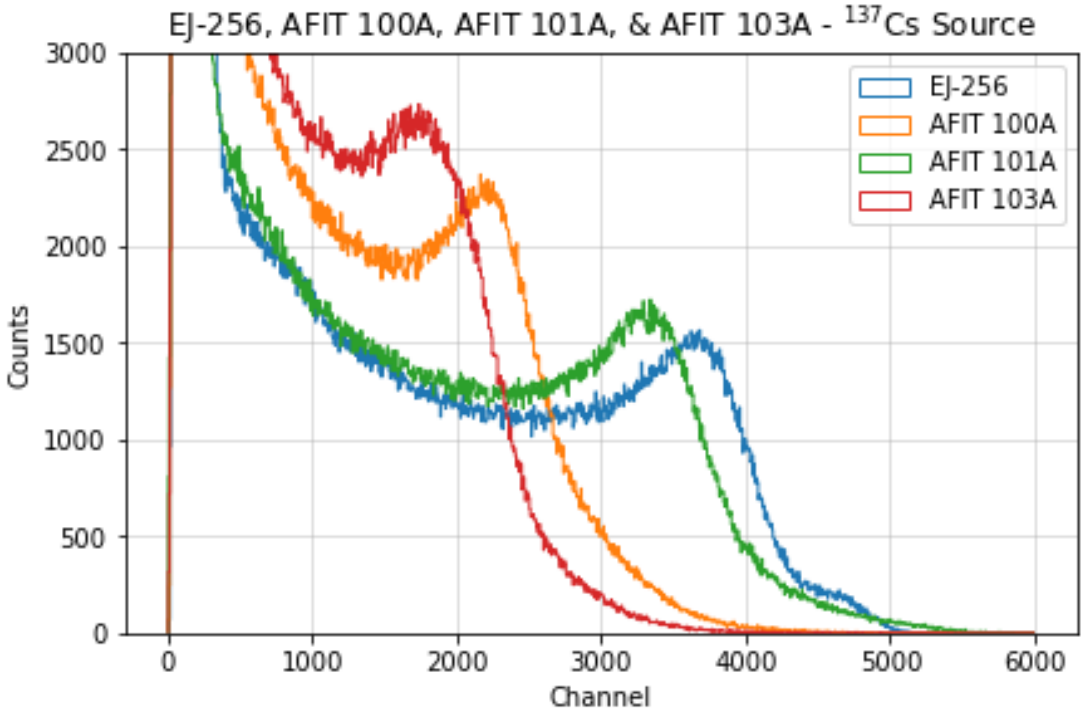

Figure 34: AFIT A-Series & EJ-256 Energy Spectra with ^{137}Cs Source

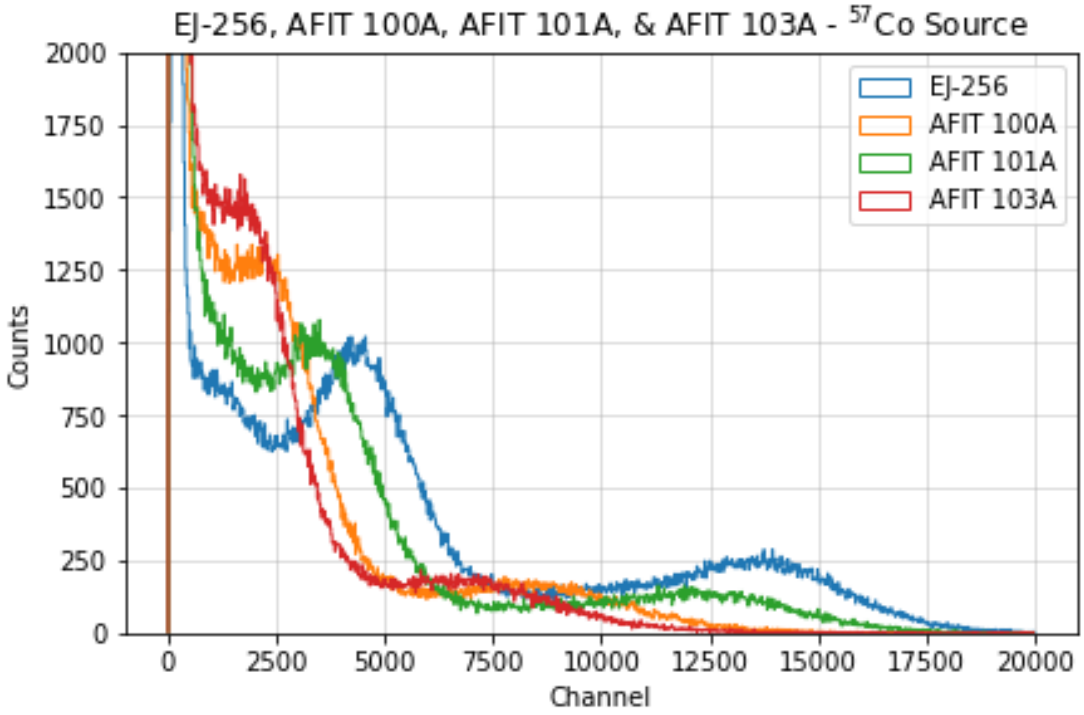

Figure 35: AFIT A-Series & EJ-256 Energy Spectra with ^{57}Co Source

The general trends elucidated by the energy histograms of the AFIT A-series scintillators when using these two radioactive sources were determined by the metrics introduced in Chapter II. Among this set of samples, the scintillator with a TPO concentration of 0.05 wt% (AFIT 101A) demonstrates the greatest light yield but the least improvement in photon detection efficiency when compared with the scintillators with both higher (0.20 wt%) and lower (0.01 wt%) TPO concentrations. The scintillator with the highest TPO concentration of 0.20 wt% (AFIT 103A) exhibits the greatest detection efficiency and the poorest light yield.

The energy histogram spectra of the AFIT B-series scintillators (i.e., AFIT 100B and AFIT 101B) with ^{137}Cs and ^{57}Co are provided in Figures 36 and 37, respectively. AFIT 102B and AFIT 103B were not characterized because significant cracks formed within them during the curing process, and the presence of those cracks preclude the collection of useful spectroscopic data.

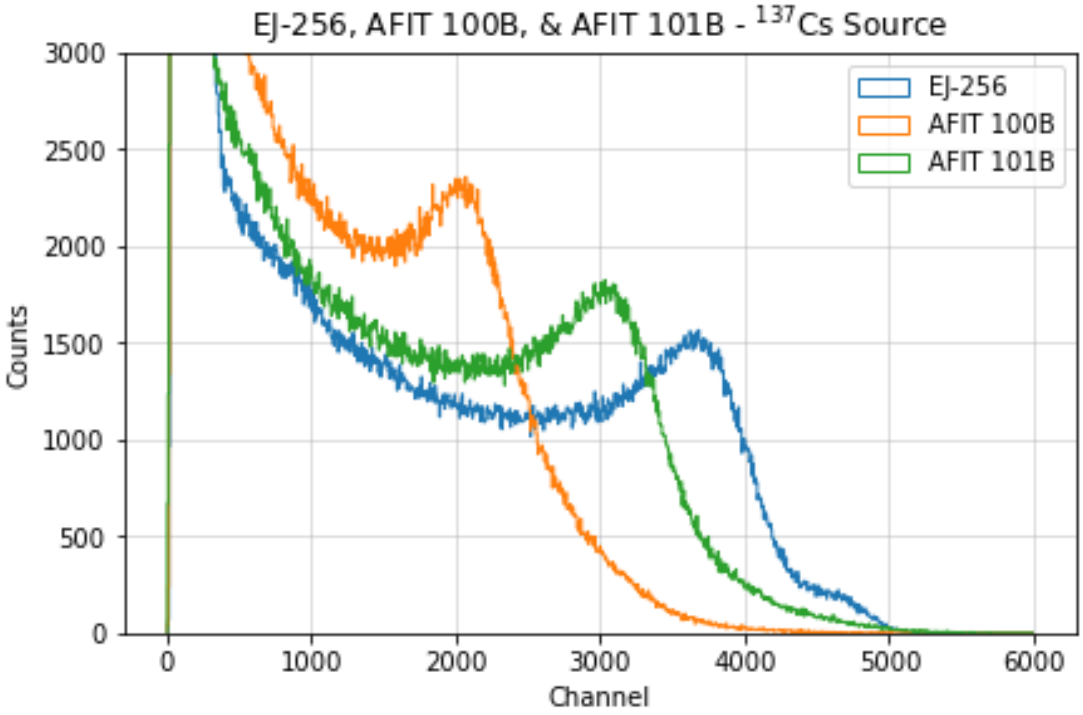

Figure 36: AFIT B-Series & EJ-256 Energy Spectra with ^{137}Cs Source

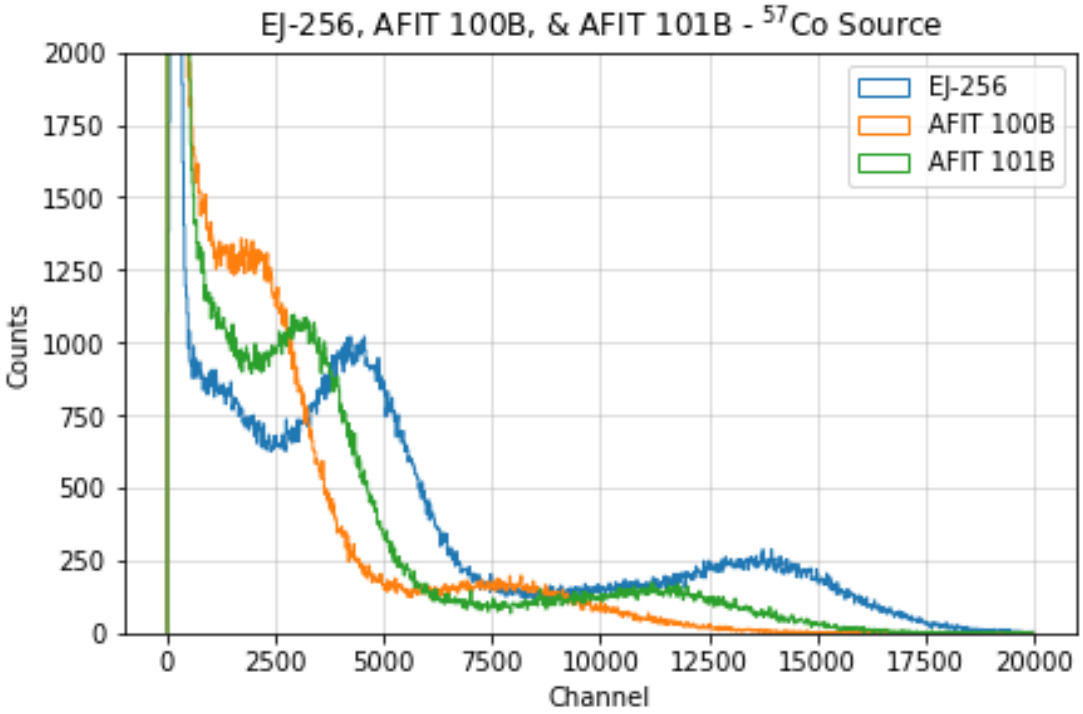

Figure 37: AFIT B-Series & EJ-256 Energy Spectra with ^{57}Co Source

General trends observed from the measured data of the AFIT B-series scintillators suggest the scintillator with a TPO concentration of 0.05 wt% (AFIT 101B) again demonstrates the greatest light yield and the lowest improvement to photon detection efficiency when compared to the scintillator with lower (0.01 wt%) TPO concentration. These findings are consistent with those observed for the A-series samples reported previously.

The measured energy histogram spectra for the AFIT C-series scintillators (i.e., AFIT 100C, AFIT 101C, and AFIT 102C) using ^{137}Cs and ^{57}Co are provided in Figures 38 and 39, respectively. AFIT 103C was not characterized, again due to cracks that formed during the curing process.

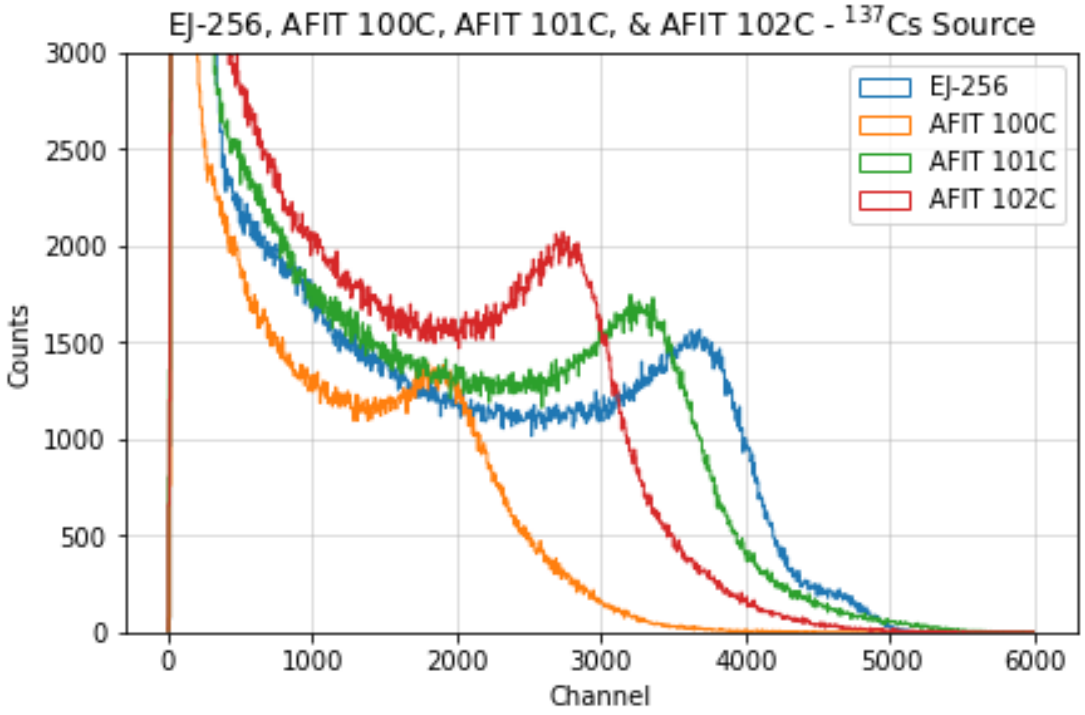

Figure 38: AFIT C-Series & EJ-256 Energy Spectra with ^{137}Cs Source

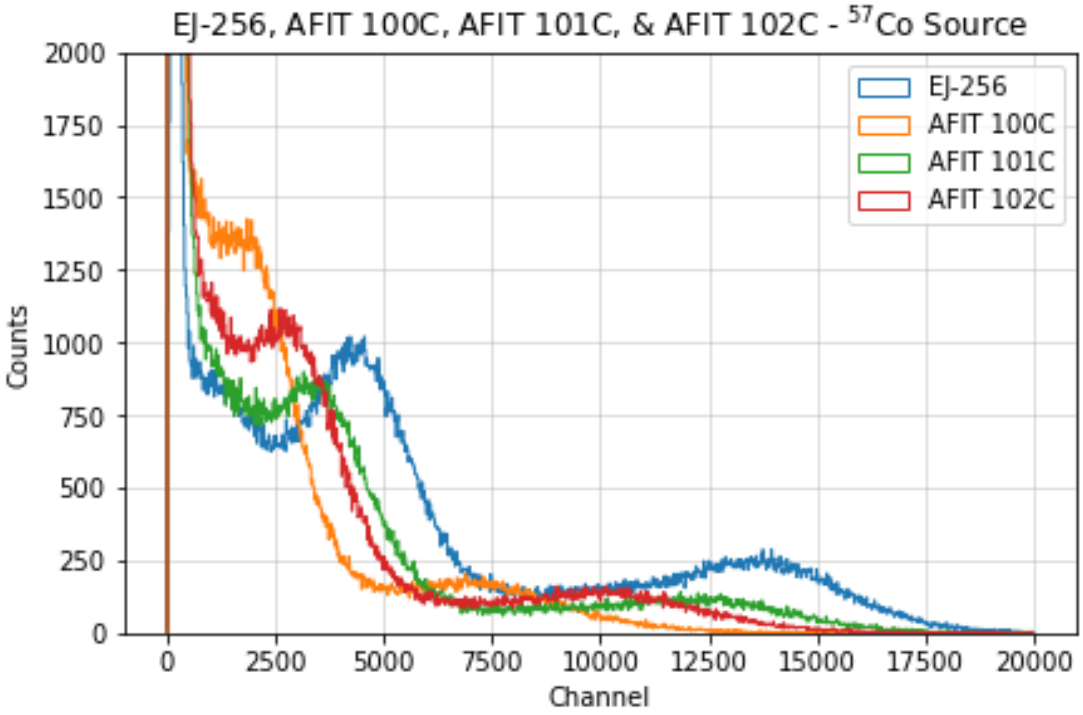

Figure 39: AFIT C-Series & EJ-256 Energy Spectra with ^{57}Co Source

The general trends elucidated by the energy histograms of the AFIT C-series scintillators suggest that the scintillator with a TPO concentration of 0.05 wt% (AFIT 101C) demonstrates the greatest light yield and the scintillator with the lowest TPO concentration (0.01 wt%) demonstrates the poorest light yield. There does not appear to be a general trend regarding which TPO concentration is associated with either the greatest or least improvement in photon detection efficiency.

The measured energy histogram spectra for the AFIT 100-series scintillators (i.e., AFIT 100A, AFIT 100B, and AFIT 100C) using ^{137}Cs and ^{57}Co are provided in Figures 40 and 41, respectively.

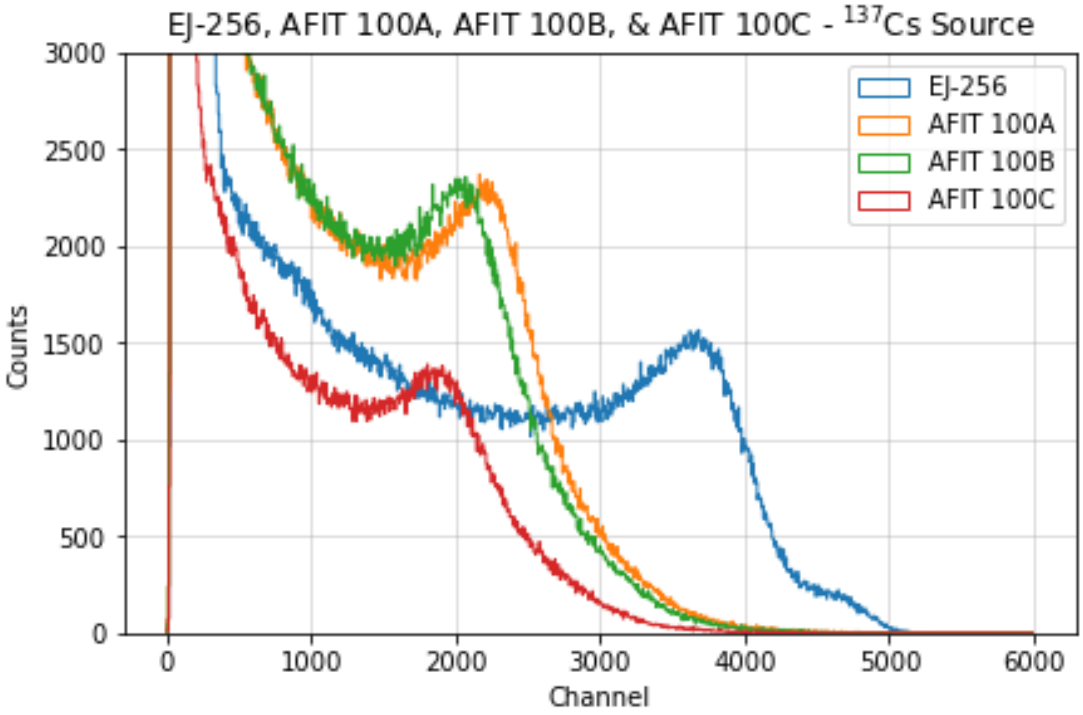

Figure 40: AFIT 100-Series & EJ-256 Energy Spectra with ^{137}Cs Source

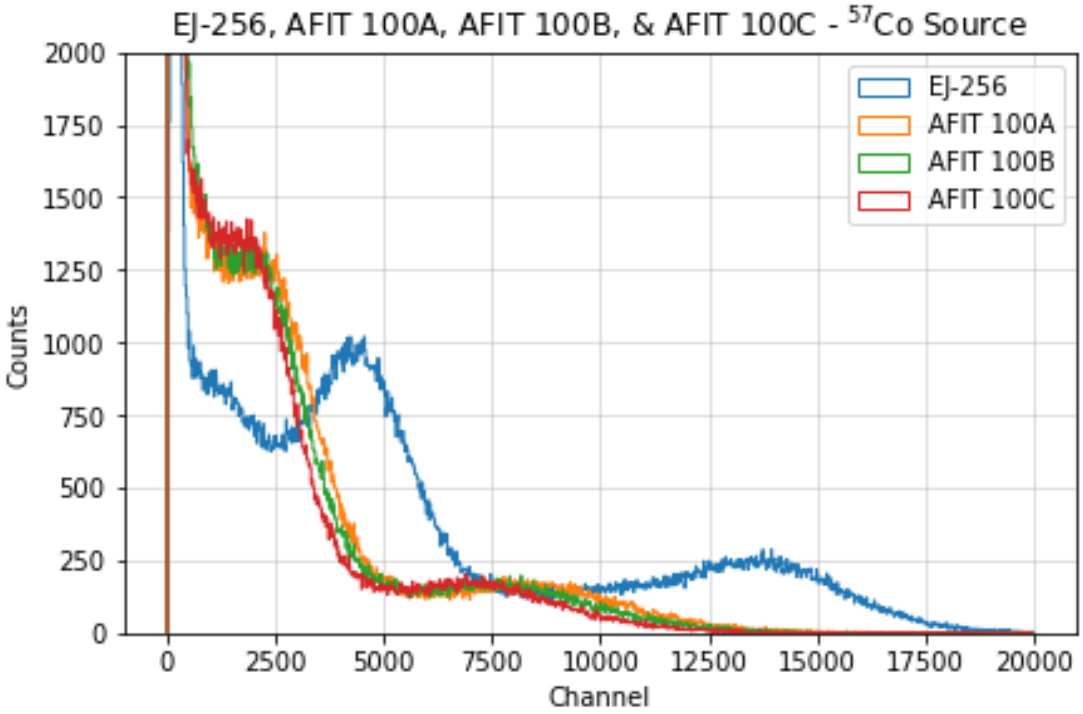

Figure 41: AFIT 100-Series & EJ-256 Energy Spectra with ^{57}Co Source

The spectra measured using the AFIT 100-series are remarkably similar with the ^{57}Co source, all with lower sensitivity and light yield at the photopeak as compared to EJ-256. Regarding the ^{137}Cs spectra, AFIT 100C is a significant outlier and the reason for this is not yet understood. AFIT 100A and AFIT 100B both exhibit higher counts at the Compton edge, indicating greater sensitivity, but at a lower corresponding channel, indicating lower light yield. Notwithstanding the anomolous AFIT 100C data with ^{137}Cs, the general trend appears to indicate that curing time beyond nine minutes (five minutes with the Formlabs Form Cure and four minutes with the Dymax BlueWave) does not produce a significant impact on scintillator performance in terms of either light yield or efficiency.

The measured energy histogram spectra for the AFIT 101-series scintillators (i.e., AFIT 101A, AFIT 101B, and AFIT 101C) using ^{137}Cs and ^{57}Co are provided in Figures 42 and 43, respectively.

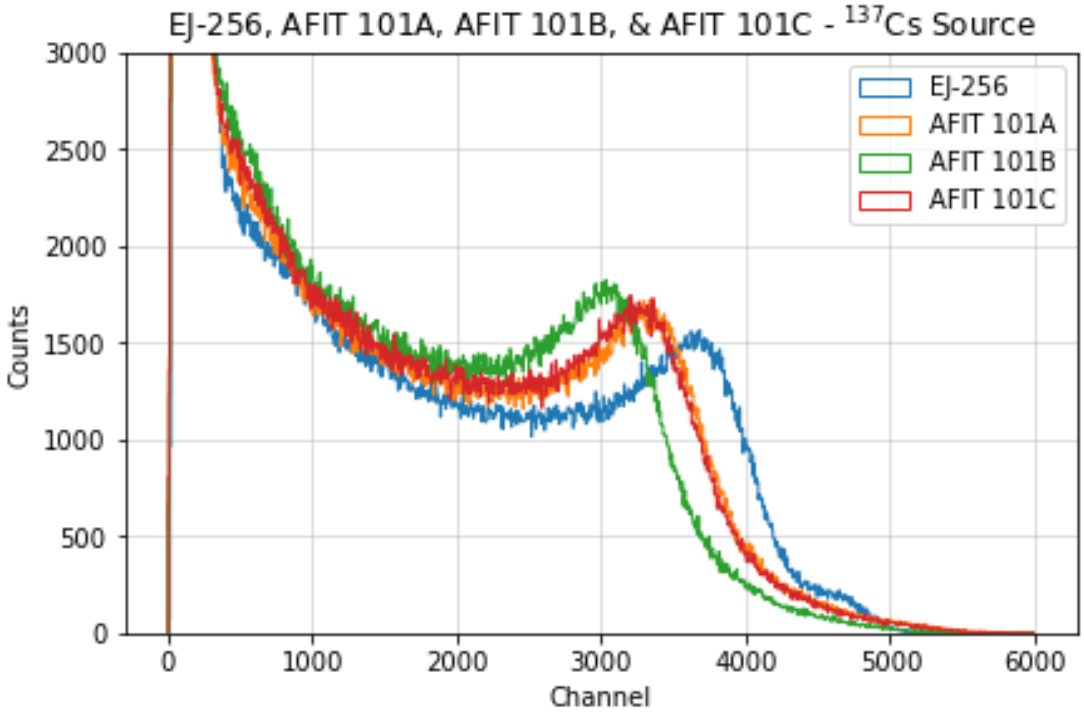

Figure 42: AFIT 101-Series & EJ-256 Energy Spectra with ^{137}Cs Source

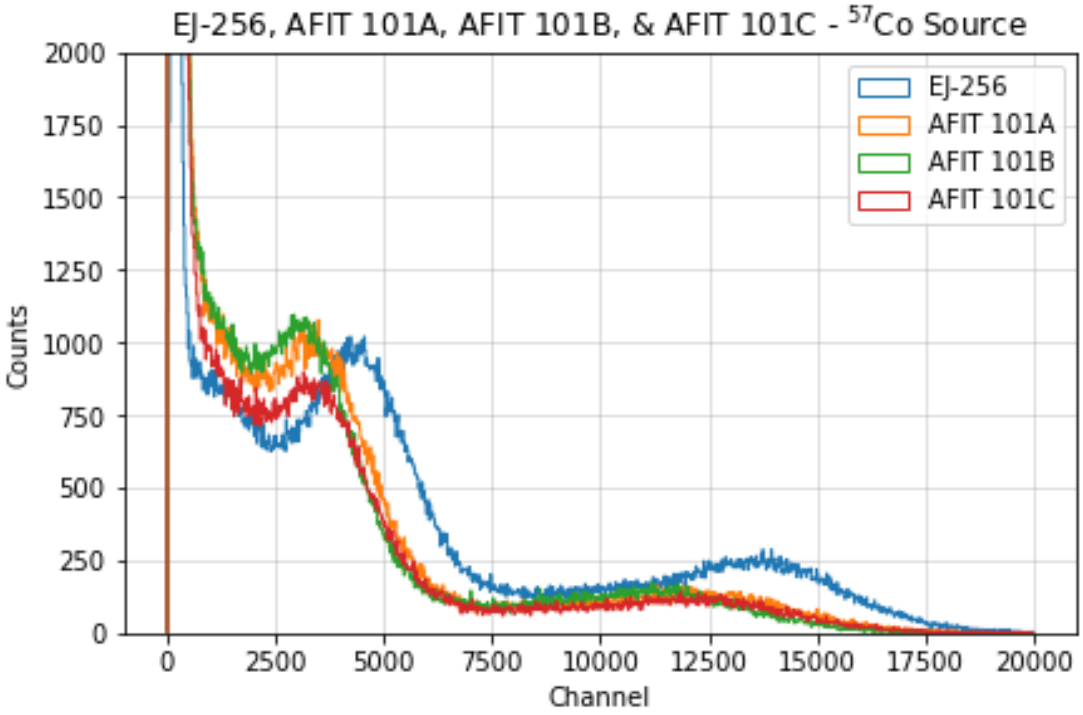

Figure 43: AFIT 101-Series & EJ-256 Energy Spectra with ^{57}Co Source

The AFIT 101-series energy spectra are also remarkably similar, with light yield very close to, if just slighty poorer than, that of EJ-256. Efficiency at the ^{57}Co photopeak is only approximately half that of EJ-256, but efficiency at the ^{137}Cs Compton edge appears to be very close to that of EJ-256.

Tables 25 and 26 provide relative metrics of measured light yield and efficiency for the samples as compared to the equivalent-sized scintillator made from EJ-256.

Table 25: Relative Light Yield Compared to EJ-256

	^{137}Cs				^{57}Co			
	100	101	102	103	100	101	102	103
A	0.63	0.92		0.55	0.58	0.88		0.42
B	0.60	0.85			0.59	0.81		
C	0.56	0.91	0.77		0.50	0.93	0.74	

Table 26: Relative Efficiency Compared to EJ-256

	^{137}Cs				^{57}Co			
	100	101	102	103	100	101	102	103
A	1.53	1.09		1.67	0.66	0.56		0.72
B	1.52	1.18			0.67	0.59		
C	0.87	1.09	1.35		0.70	0.47	0.63	

4.3.3 Expected Results Compared to Measured Performance

The initial expectation was that the light yield would decrease and sensitivity would increase with increasing TPO content. This is because it was postulated that TPO may remain in the scintillator in an amount that is in excess of what was required to successfully complete the curing process. Given that TPO is a light-sensitive compound, which is a necessary characteristic for any photoinitiator, it was hypothesized that any TPO that might remain in the cured scintillator may exist in a form that provides an additional means of interaction with photons. This additional source of interactions in scintillators with higher TPO loadings was, therefore, associated with decreasing light yield and increasing sensitivity. The most consistent deviation from this hypothesized trend is reflected in the lower than expected values of measured light yield for the AFIT 100-series scintillators, which had the lowest TPO concentration of 0.01 wt%. However, it is assessed that the presence of extensive surface fissuring, which afflicted all of the AFIT 100-series scintillators, directly contributed to this measured result. The extensive cracking present on the surfaces of these scintillators obviously contributes to reduced light transmissivity across the surface and interferes with the path and reflection of scintillation photons, thereby diminishing measured light yield. Notwithstanding the anomalous behavior of the AFIT 100-series, the general trend of higher sensitivity with greater TPO concentration tended to remain consistent.

V. Conclusions

5.1 Key Findings

There have been many useful findings from this investigation. Some of these findings were expected and others were not. Lessons learned from this investigation may inform future investigations into fast-curing, high-Z-loaded plastic scintillators.

Many of the findings regarding physical characteristics of the scintillators were quite unexpected. For example, lowering the photoinitiator concentration significantly still enabled the fabrication of scintillators that are hard and durable enough to withstand the mechanical stresses of the finishing process. The observed slower rate of heat buildup in these scintillators during the curing process, which was qualitatively correlated with reduced TPO concentration, creates the possibility of reducing cooling time between curing iterations. This finding is expected to decrease the likelihood of cracking in future fast-curing formulations and may also facilitate the formulation of larger scintillator volumes at speed.

The findings regarding scintllator relative performance are also promising. This study established that high-Z loading of fast-curing, acrylic-based plastic scintillators is possible, and these follow the anticipated trends in diminished light yield and increased photon sensitivity at greater high-Z loadings, as shown in previous literature. More importantly, optimal curing times and TPO loadings for high-Z loaded novel samples have been explored and refined, with early samples demonstrating overall performance (both light yield and photon sensitivity) that nearly matches that of industry standards, such as EJ-256.

Given that none of the curing time protocols revealed any significant advantages over the others, the minimum cure time of nine minutes (i.e., five minutes of curing with the Formlabs Form Cure and four minutes of curing with the Dymax BlueWave),

which corresponded to the AFIT A-series curing protocol, appears to be ideal for economy of time and resources. The AFIT 101-series (with 5 wt% TPO loading) easily outperformed the other TPO loading concentrations, primarily due to lack of residual purple coloring and absence of surface fissuring. The AFIT 101-series, however, was slightly (but noticeably) tinged yellow as compared to the AFIT 100-series. The conjecture is that there is an optimal TPO loading somewhere between 0.01 and 0.05 wt% TPO, which is high enough to preclude surface fissuring and low enough to maximize light yield. Given that many of the same characteristics associated with a 0.1 wt% TPO content (i.e., purpling, cracking, and heat buildup during curing) were also present in similar formulations with no high-Z loading [1], it is likely that reduction in TPO content could have favorable effects for both high-Z loaded and non-high-Z loaded formulations.

Based upon the new information revealed in this investigation regarding physical attributes and detection performance, AFIT 101A appears to be the most favorable candidate for further study and refinement. The hardness, clarity, lack of coloration, lack of curing-induced cracking, absence of surface fissuring, slow rate of heating during curing, appreciable photon sensitivity, and decent light yield all contribute to making this scintillator an attractive option for development. As noted previously, a slightly lower TPO content (e.g., 0.02 or 0.03 wt%) would seem to be a logical proposed modification to optimize physical and performance factors.

5.2 Future Work

The surface fissuring of the scintillators with the lowest photoinitiator content indicate that an ideal TPO concentration exists, likely between 0.01 wt% and 0.05 wt%, that is just high enough to prevent this surface cracking from occurring and low enough to retain the favorable effects of low TPO content. Fine-tuning this

concentration could optimize physical characteristics, such as requisite hardness and longevity, and performance metrics, such as light yield.

There is much evidence of inorganic compounds being successfully employed for increasing photon sensitivity of plastic scintillators. More recent literature on this subject specifically mentions the use of nanoparticles, which are currently prohibited in the available laboratories due to safety regulations. If access to facilities can be gained where use of nanoparticles is permitted, the pool of available compounds for potentially increasing scintillator sensitivity increases appreciably. There is also a sizeable selection of organic high-Z compounds that could potentially be used in novel formulations, with the aim of finding a compound that minimally decreases light yield while maximally increasing photon sensitivity. Exploring the lower limit of plastic content (i.e., the monomer and crosslinker components) can create more possibilities for adding higher concentrations of other materials to scintillator formulations that will improve or optimize their performance in other ways. The vast majority of scintillators produced in this investigation contain 63 wt% plastic, but some as low as 56 wt% have been produced that exhibit adequate hardness, and even lower proportions of plastic may be achievable. Since many previous non-high-Z loaded formulations exhibited inadequate hardness below 60 wt% plastic [1], the high-Z component may be positively correlated with hardness.

Lastly, the goal of additive manufacturing with fast-curing formulations appears within reach. Prototypes of 3D-printed fast-curing plastic scintillators have been recently produced using unsensitized formulations [47]. With further refinements, high-Z loaded formulations are likely not far behind. As the state of the art of additively manufacturing fast-curing plastic scintillators evolves, the follow-on goal of 3D printing plastic pixelated arrays is closer to fruition.

Bibliography

1. B. G. Frandsen. Phd dissertation (under review), 2021.

2. Seals Unlimited. Decoding basic rubber hardness durometer scales. https://www.sealsunlimited.com/seals.nsf/weblinks/AHBD-AA23P8?open, 2022. Accessed on 2022-03-12.

3. T. J. Hajagos, N. J. Cherepy C. Liu, and Q. Pei. High-z sensitized plastic scintillators: A review. *Advanced Materials*, 30(1706956), 2018.

4. Inc. Ludlum Measurements. Portal monitors. https://ludlums.com/products/medical-physics/category/portal-monitors-mp, 2022. Accessed on 2022-03-12.

5. Saint-Gobain Crystsals. Extended life plastic. https://www.crystals.saint-gobain.com/radiation-detector-assemblies/extended-life-plastic-packaging, 2021. Accessed on 2022-03-12.

6. A. W. Decker, C. J. Delzer, S. Hok, N. J. Cherepy, and J. P. Hayward. X-ray radiography characterization using a bismuth-loaded polyvinyltoluene array. *Journal of Radiation Effects, Research and Engineering*, 39(1):11–21, 2021.

7. E. J. Lerner. Photomultiplier tubes offer high-end sensitivity. https://www.laserfocusworld.com/detectors-imaging/article/16548987/photomultiplier-tubes-offer-highend-sensitivity, 1996. Accessed on 2021-08-26.

8. Saint-Gobain Crystals. Pixellated arrays. https://www.crystals.saint-gobain.com/radiation-detector-assemblies/pixellated-arrays, 2021. Accessed on 2022-02-20.

9. A. W. Decker, N. J. Cherepy, S. Hok, and J. P. Hayward. Simulated x-ray radiographic performance of a bismuth-loaded pvt array. *IEEE Transactions on Nuclear Science*, 67(11):2329–2336, 2020.

10. Inc. Varian Medical Systems. Methods for fabricating pixelated scintillator arrays. https://patents.justia.com/patent/10145966citations, 2015. Accessed on 2022-03-12.

11. A. Lim, A. Mahl, J. Latta, H. A. Yemam, U. Grelfe, and A. Sellinger. Plastic scintillators with efficient light output and pulse shape discrimination produced via photoinitiated polymerization. *Journal of Applied Polymer Science*, 2018.

12. Eljen Technology. Plastic scintillators. https://eljentechnology.com/products/plastic-scintillators/, 2021. Accessed on 2021-08-26.

13. McMaster University. Med phys 4r06/6r03 - radioisotopes and radiation methodology: Chapter 4 scintillation detectors. https://www.science.mcmaster.ca/radgrad/images/6R06CourseResources/4R6Notes4_ScintillationDetectors.pdf, 2022. Accessed on 2022-03-12.

14. J. B. Birks. *The Theory and Practice of Scintillation Counting*. Pergamon Press, 1st edition, 1964.

15. Pieter Dorenbos. (invited) the quest for high resolution -ray scintillators. *Optical Materials: X*, 1:100021, 2019.

16. Saint-Gobain Crystals. Nai(tl) scintillation crystal. https://www.crystals.saint-gobain.com/radiation-detection-scintillators/crystal-scintillators/naitl-scintillation-crystals, 2021. Accessed on 2022-02-21.

17. M. Miyajima, S. Sasaki, and H. Tawara. Numbers of scintillation photons produced in NaI(Tl) and plastic scintillator by gamma-rays. *IEEE Trans. Nucl. Sci.*, 40:417–423, 1993.

18. Shinichi Sasaki, Hiroko Tawara, Kiwamu Saito, Mitsuhiro Miyajima, and Eido Shibamura. Average energies required per scintillation photon and energy resolutions in NaI(tl) and CsI(tl) crystals for gamma rays. *Japanese Journal of Applied Physics*, 45(8A):6420–6430, aug 2006.

19. Glenn F. Knoll. *Radiation detection and measurement*. Wiley, 4th edition, 2010.

20. Columbia University. Liquid scintillation counter user manual. https://research.columbia.edu/sites/default/files/content/EHS/Rad%20Safety/LSCUserManual.pdf, 2021. Accessed on 2022-02-20.

21. Wikipedia. Photomultiplier tube. https://en.wikipedia.org/wiki/Photomultiplier_tube, 2022. Accessed on 2022-03-12.

22. Eljen Technology. Liquid scintillators. https://eljentechnology.com/products/liquid-scintillators, 2022. Accessed on 2022-01-18.

23. Alice Tomanin, Jan Paepen, P. Schillebeeckx, Ruud Wynants, Ralf Nolte, and Anthony Lavietes. Characterization of a cubic ej-309 liquid scintillator detector. *Nuclear Instruments and Methods in Physics Research A*, 756:45–54, 08 2014.

24. W. A. Green. Boosting the cure of phosphine oxide photoinitiators. sensitisation or synergy? *RadTech UV & EB Technical Conference Proceedings*, 2016.

25. G. Bertrand, F. Sguerra, Chrystele Dehe-Pittance, F. Carrel, R. Coulon, S. Normand, E. Barat, T. Dautremer, T. Montagu, and M. Hamel. Influence of bismuth loading in polystyrene-based plastic scintillators for low energy gamma spectroscopy. *Journal of Materials Chemistry C*, 2:7304–7312, 2014.

26. Z. H. Cho, C. M. Tsai, and L. A.Eriksson. Tin and lead loaded plastic scintillators for low energy gamma-ray detection with particular application to high rate detection. *IEEE Transactions on Nuclear Science*, 22(1):72–80, 1975.

27. Sean P. O'Neal, Nerine J. Cherepy, Saphon Hok, and Stephen Payne. High-light yield bismuth-loaded plastic scintillators. In Nerine J. Cherepy, Michael Fiederle, and Ralph B. James, editors, *Hard X-Ray, Gamma-Ray, and Neutron Detector Physics XXIII*, volume 11838. International Society for Optics and Photonics, SPIE, 2021.

28. Center for Applied Isotope Studies University of Georgia. X-ray fluorescence. http://cais.uga.edu/wp-content/uploads/2019/01/XRF_Background.pdf, 2019. Accessed on 2022-03-03.

29. B. L. Rupert, N. J. Cherepy, B. W. Sturm, R. D. Sanner, and S. A. Payne. Bismuth-loaded plastic scintillators for gamma-ray spectroscopy. *EPL (Europhysics Letters)*, 97(2):22002, jan 2012.

30. M. W. Davidson and The Florida State University. Fluorescence microscopy interactive java tutorials: Jablonski energy diagram. https://micro.magnet.fsu.edu/primer/java/jablonski/jabintro/index.html, 2017. Accessed on 2022-03-12.

31. Stephen A. Payne, William W. Moses, Steven Sheets, Larry Ahle, Nerine J. Cherepy, Benjamin Sturm, Steven Dazeley, Gregory Bizarri, and Woon-Seng Choong. Nonproportionality of scintillator detectors: Theory and experiment. ii. *IEEE Transactions on Nuclear Science*, 58(6):3392–3402, 2011.

32. H. Schneckenburger. Förster resonance energy transfer–what can we learn and how can we use it? *Methods and Applications in Fluorescence*, 8(013001), 2020.

33. AAT Bioquest. Spectrum [ppo]. https://www.aatbio.com/fluorescence-excitation-emission-spectrum-graph-viewer/PPO, 2021. Accessed on 2022-02-21.

34. S. Prahl. 2,5-diphenyloxazole, [ppo]. https://omlc.org/spectra/PhotochemCAD/html/020.html, 2017. Accessed on 2022-02-21.

35. L. Pandiscia. Evaluation of fret as a sensitive biosensor for explosives. https://jascoinc.com/applications/sensitivity-evaluation-of-a-biosensor-using-fret/, 2017. Accessed on 2022-03-12.

36. Exciton Luxottica. Exalite 416 datasheet. https://exciton.luxottica.com/pub/media/productattach/Datasheet/04160.pdf, 2022. Accessed on 2022-02-21.

37. Photonic Solutions. Exciton laser dyes. https://photonicshop.co.uk/products/exciton-laser-dyes-a-f, 2022. Accessed on 2022-02-21.

38. Virgil Taillandier. *High speed imaging detectors with diamond dynode materials.* PhD thesis, 10 2013.

39. Thibault Laplace, B.L. Goldblum, J.A. Brown, and Juan Manfredi. Scintillator light yield measurements with waveform digitizers. *Nuclear Instruments and Methods in Physics Research Section A: Accelerators, Spectrometers, Detectors and Associated Equipment*, 959:163485, 02 2020.

40. Nicholas Tsoulfanidis and Sheldon Landsberger. *Measurement detection of radiation.* CRC Press, Taylor Francis Group, 4th edition, 2015.

41. Hamamatsu Photonics K.K. Photomultiplier tube r7723, r7724, r7725. https://www.hamamatsu.com/resources/pdf/etd/R7723_R7724_R7725_TPMH1315E.pdf, 2021. Accessed on 2022-01-18.

42. CAEN S.p.A. Dt5730 / dt5730s 8 channel 14 bit 500 ms/s digitizer. https://www.caen.it/products/dt5730/, 2021. Accessed on 2021-09-07.

43. CAEN S.p.A. Dt5533e 4 channel 4 kv/3 ma (4 w) desktop hv power supply module (usb/ethernet). https://www.caen.it/products/dt5533e/, 2021. Accessed on 2021-09-07.

44. CAEN S.p.A. Compass multiparametric daq software for physics applications. https://www.caen.it/products/compass/, 2021. Accessed on 2021-09-07.

45. CAEN S.p.A. Geco2020 general control software for caen hv power supplies. https://www.caen.it/products/geco2020/, 2021. Accessed on 2021-09-07.

46. N. P. Zaitseva, A. M. Glenn, A. N. Mabe, M. L. Carman, C. R. Hurlbut, J. W. Inman, and S. A. Payne. Recent developments in plastic scintillators with pulse shape discrimination. *Nuclear Inst. and Methods in Physics Research, A*, 2018.

47. M. T. Febbraro. Unpublished research, 2022.

Acronyms

BPADM bisphenol A dimethacrylate. 11

DIPN diisopropyl naphthalene. 13

DPI dual-particle imaging. 1

FRET Förster Resonance Energy Transfer. 23

HDDMA 1,6-hexanediol dimethacrylate. 11

IBOA isobornyl acrylate. 11

MeVee mega-electron volt electron equivalent. 22

PPO 2,5-diphenyl oxazole. 13

PS polystyrene. 3, 11

PSD pulse shape discrimination. 13

PTFE polytetrafluoroethylene. 41

PVT polyvinyl toluene. 3, 11

TPO diphenyl (2,4,6-trimethylbenzoyl) phosphine oxide. 14

TTA triplet-triplet annihilation. 21

REPORT DOCUMENTATION PAGE

Form Approved
OMB No. 0704–0188

1. REPORT DATE *(DD–MM–YYYY)*	2. REPORT TYPE	3. DATES COVERED *(From — To)*
24–03–2022	Master's Thesis	Sep 2020 - Mar 2022

4. TITLE AND SUBTITLE

Formulation and Characterization of Fast-Curing Plastic Scintillators with High-Z Loading

5a. CONTRACT NUMBER

5b. GRANT NUMBER

5c. PROGRAM ELEMENT NUMBER

6. AUTHOR(S)

Stephens, Theodore W., Lieutenant Colonel

5d. PROJECT NUMBER

5e. TASK NUMBER

5f. WORK UNIT NUMBER

7. PERFORMING ORGANIZATION NAME(S) AND ADDRESS(ES)

Air Force Institute of Technology
Graduate School of Engineering and Management (AFIT/EN)
2950 Hobson Way
Wright-Patterson AFB, OH 45433-7765

8. PERFORMING ORGANIZATION REPORT NUMBER

AFIT-ENP-MS-22-M-112

9. SPONSORING / MONITORING AGENCY NAME(S) AND ADDRESS(ES)

Defense Threat Reduction Agency

10. SPONSOR/MONITOR'S ACRONYM(S)

DTRA

11. SPONSOR/MONITOR'S REPORT NUMBER(S)

12. DISTRIBUTION / AVAILABILITY STATEMENT

DISTRIBUTION STATEMENT A:
APPROVED FOR PUBLIC RELEASE; DISTRIBUTION UNLIMITED.

13. SUPPLEMENTARY NOTES

14. ABSTRACT

Development of novel fast-curing plastic scintillators is highly advantageous due to their potential to be manufactured via 3D printing. Several formulations were developed that exhibit enhanced photon sensitivity, producing modest but discernible photopeaks at an incident gamma energy of 122 keV. The photon sensitivity is achieved via bismuth high-Z loading; however, this practice typically results in diminished light yields. Subsequent formulations, which varied the photoinitiator concentration and curing time, demonstrated successful curing with sufficient plastic hardness, reduced purple discoloration, reduced heat buildup during curing, and resulted in less cracking during the curing process, all of which were correlated with lower concentrations of the photoinitiator. These scintillators, however, did exhibit appreciable leaching of the primary fluorophore. As compared to EJ-256 with ^{137}Cs and ^{57}Co sources, relative light yield was generally slightly poorer, ranging from 42% to 93%, and relative efficiency was generally comparable, ranging from 47% to 167%.

15. SUBJECT TERMS

Organic Scintillator, Bismuth, High-Z Loading, Plastic Scintillator, Fast-Curing

16. SECURITY CLASSIFICATION OF:			17. LIMITATION OF ABSTRACT	18. NUMBER OF PAGES	19a. NAME OF RESPONSIBLE PERSON
a. REPORT	b. ABSTRACT	c. THIS PAGE			LTC Andrew W. Decker, AFIT/ENP
U	U	U	UU	88	19b. TELEPHONE NUMBER *(include area code)* (937) 255-3636 x4611; andrew.decker@afit.edu